Role of diquark correlations and the pion cloud in nucleon elastic form factors

Ian C. Cloët,[1] Wolfgang Bentz,[2] and Anthony W. Thomas[3]
[1]*Physics Division, Argonne National Laboratory, Argonne, Illinois 60439, USA*
[2]*Department of Physics, School of Science, Tokai University, Hiratsuka-shi, Kanagawa 259-1292, Japan*
[3]*CSSM and ARC Centre of Excellence for Particle Physics at the Terascale, School of Chemistry and Physics, University of Adelaide, Adelaide, South Australia 5005, Australia*
(Received 29 May 2014; published 6 October 2014)

Electromagnetic form factors of the nucleon in the spacelike region are investigated within the framework of a covariant and confining Nambu–Jona-Lasinio model. The bound-state amplitude of the nucleon is obtained as the solution of a relativistic Faddeev equation, where diquark correlations appear naturally as a consequence of the strong coupling in the color $\bar{3}$ qq channel. Pion degrees of freedom are included as a perturbation to the "quark-core" contribution obtained using the Poincaré covariant Faddeev amplitude. While no model parameters are fit to form-factor data, excellent agreement is obtained with the empirical nucleon form factors (including the magnetic moments and radii) where pion loop corrections play a critical role for $Q^2 \lesssim 1$ GeV^2. Using charge symmetry, the nucleon form factors can be expressed as proton quark sector form factors. The latter are studied in detail, leading, for example, to the conclusion that the d-quark sector of the Dirac form factor is much softer than the u-quark sector, a consequence of the dominance of scalar diquark correlations in the proton wave function. On the other hand, for the proton quark sector Pauli form factors we find that the effect of the pion cloud and axial-vector diquark correlations overcomes the effect of scalar diquark dominance, leading to a larger d-quark anomalous magnetic moment and a form factor in the u-quark sector that is slightly softer than in the d-quark sector.

DOI: 10.1103/PhysRevC.90.045202 PACS number(s): 13.40.Em, 13.40.Gp, 25.30.Bf, 24.85.+p

I. INTRODUCTION

The electromagnetic form factors of a nucleon provide information on its internal momentum space distribution of charge and magnetization, thus furnishing a unique window into the quark and gluon substructure of the nucleon. Building a bridge between QCD and the observed nucleon properties is a key challenge for modern hadron physics and recent form-factor measurements, for example, demonstrate that a robust understanding of nucleon properties founded in QCD is just beginning.

A key example of the impact of such measurements is provided by the polarization transfer experiments [1–6], which revealed that the ratio of the proton's electric to magnetic Sachs form factors, $\mu_p\, G_{Ep}(Q^2)/G_{Mp}(Q^2)$, is not constant but instead decreases almost linearly with Q^2. These experiments dispelled decades of perceived wisdom which perpetuated the view that the nucleon contained similar distributions of charge and magnetization. Nucleon form-factor data at large Q^2 can also be used to test the scaling behavior predicted by perturbative QCD, which, for example, makes the prediction that $Q^2\, F_{2p}(Q^2)/F_{1p}(Q^2)$ should tend to a constant as $Q^2 \to \infty$ [7,8]. However, recent data extending to $Q^2 \simeq 8$ GeV^2 [5,6] find scaling behavior much closer to $Q\, F_{2p}(Q^2)/F_{1p}(Q^2)$, which has been attributed to the quark component of the nucleon wave function possessing sizable orbital angular momentum [9]. An interesting recent example, which demonstrates that there is much of a fundamental nature still to learn in hadron physics, involves the muonic hydrogen experiments [10,11] that found a proton charge radius some 4% smaller than that measured in elastic electron scattering or electronic hydrogen, representing a 7σ discrepancy. As yet there is no accepted resolution to this puzzle [12–14].

It is clear, therefore, that a quantitative theoretical understanding of nucleon form factors in terms of the fundamental degrees of freedom of QCD, namely the quarks and gluons, remains an important goal. This task is particularly challenging because nucleon form factors parametrize the amplitude for a nucleon to interact through a current and remain a nucleon for arbitrary spacelike momentum transfer. Therefore, long-distance nonperturbative effects associated with quark binding and confinement must play an important role at all Q^2, while, because of asymptotic freedom at short distances, perturbative QCD must also be relevant at large momentum transfer. This scenario is somewhat in contrast to that found with the structure functions measured in deep inelastic scattering, which can be factorized into short-distance Wilson coefficients, calculable in perturbative QCD, and the long-distance parton distribution functions (PDFs) which encode nonperturbative information on the structure of the bound state. A consequence of factorization is that once the PDFs are known at a scale $Q_0^2 \gg \Lambda^2_{\rm QCD}$, the Q^2 evolution of the PDFs, on the Bjorken x domain relevant to hadron structure, is governed by the DGLAP evolution equations [15–17]. An analogous factorization is not possible for the nucleon electromagnetic form factors.

Here we investigate the nucleon electromagnetic form factors using the Nambu–Jona-Lasinio (NJL) model [18–22], which is a Poincaré covariant quantum field theory with many of the same low-energy properties as QCD. For example, it encapsulates the key emergent phenomena of dynamical chiral symmetry breaking and confinement.[1] This model also has the same flavor symmetries as QCD and should

[1]Standard implementations of the NJL model are not confining. This can be seen in results for hadron propagators which develop imaginary

therefore provide a robust chiral effective theory of QCD valid at low to intermediate energies. The NJL model is solved nonperturbatively, using the standard leading-order truncation. Finally, to respect chiral symmetry effectively, we also include pion degrees of freedom in a perturbative manner. This proves essential [23–25] for a good description of the nucleon form factors below $Q^2 \sim 1$ GeV^2.

The outline of the paper is as follows. Section II gives an introduction to the NJL model, encompassing the gap equation, the Bethe-Salpeter equation and the relativistic Faddeev equation. In Sec. III we explain how to calculate the matrix elements of the quark electromagnetic current which give the nucleon electromagnetic form factors. A key ingredient is the dressed quark-photon vertex: the interaction of a virtual photon with a nonpointlike constituent, or dressed quark, which is detailed in Sec. IV. Pion loop effects at the constituent quark level are also discussed and results for dressed quark form factors are presented. Because the nucleon emerges as a quark-diquark bound state, a critical step in determining the nucleon form factors is to determine the electromagnetic current for the relevant diquarks. This is discussed in Sec. V for scalar and axial-vector diquarks, together with form-factor results for the pion and ρ mesons, which are the $\bar{q}q$ analogs of these diquarks. The electromagnetic current of the nucleon is determined in Sec. VI, where the role of pion loop effects is discussed in detail. Careful attention is paid to the flavor decomposition of the nucleon form factors and the interpretation of their Q^2 dependence in terms of the interplay between the roles of diquark correlations and pionic effects within the nucleon. Comparisons with experiment are presented and inferences drawn regarding features of the data and connections to the quark structure within the nucleon. Conclusions are presented in Sec. VII.

II. NAMBU–JONA-LASINIO MODEL

The NJL model, while originally a theory of elementary nucleons [18,19], is now interpreted as a QCD-motivated chiral effective quark theory characterized by a 4-fermion contact interaction between the quarks [20–22]. A salient feature of the model is that it is a Poincaré covariant quantum field theory where interactions dynamically break chiral symmetry, giving rise to dynamically generated dressed quark masses, a pion that is a $\bar{q}q$ bound state with the properties of a pseudo-Goldstone boson and a large mass splitting between low-lying chiral partners. The NJL model has a long history of success in the study of meson properties [20,22] and more recently as a tool to investigate baryons as 3-quark bound states using the relativistic Faddeev equation [26–28]. Recent examples include the study of nucleon PDFs [29–33], quark fragmentation functions [34,35], and transverse momentum-dependent PDFs [36,37]. Finally, we mention that the NJL model has been used to study the self-consistent modification of the structure of the nucleon in-medium and its role in the binding of atomic nuclei [38].

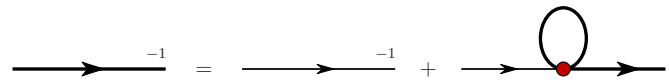

FIG. 1. (Color online) The NJL gap equation in the Hartree-Fock approximation, where the thin line represents the elementary quark propagator, $S_0^{-1}(k) = \not{k} - m + i\varepsilon$, and the shaded circle represents the $\bar{q}q$ interaction kernel given in Eq. (2). Higher-order terms, attributed to meson loops, for example, are not included in the gap equation kernel.

The SU(2) flavor NJL Lagrangian relevant to this study, in the $\bar{q}q$ interaction channel, reads[2]

$$\begin{aligned}\mathcal{L} = {} & \bar{\psi}(i\partial\!\!\!/ - \hat{m})\psi \\ & + \tfrac{1}{2}\,G_\pi[(\bar{\psi}\psi)^2 - (\bar{\psi}\,\gamma_5\vec{\tau}\,\psi)^2] - \tfrac{1}{2}\,G_\omega(\bar{\psi}\,\gamma^\mu\,\psi)^2 \\ & - \tfrac{1}{2}\,G_\rho[(\bar{\psi}\,\gamma^\mu\vec{\tau}\,\psi)^2 + (\bar{\psi}\,\gamma^\mu\gamma_5\vec{\tau}\,\psi)^2], \end{aligned} \tag{1}$$

where $\hat{m} \equiv \mathrm{diag}[m_u, m_d]$ is the current quark mass matrix and the 4-fermion coupling constants in each chiral channel are labeled by G_π, G_ω, and G_ρ. Throughout this paper we take $m_u = m_d = m$. The interaction Lagrangian can be Fierz symmetrized, with the consequence that after a redefinition of the 4-fermion couplings one need only consider direct terms in the elementary interaction [28]. The elementary quark-antiquark interaction kernel is then given by

$$\begin{aligned}\mathcal{K}_{\alpha\beta,\gamma\delta} = {} & \sum_\Omega K_\Omega\,\Omega_{\alpha\beta}\,\bar{\Omega}_{\gamma\delta} \\ = {} & 2i\,G_\pi[(\mathbb{1})_{\alpha\beta}(\mathbb{1})_{\gamma\delta} - (\gamma_5\tau_i)_{\alpha\beta}(\gamma_5\tau_i)_{\gamma\delta}] \\ & - 2i\,G_\rho[(\gamma_\mu\tau_i)_{\alpha\beta}(\gamma^\mu\tau_i)_{\gamma\delta} + (\gamma_\mu\gamma_5\tau_i)_{\alpha\beta}(\gamma^\mu\gamma_5\tau_i)_{\gamma\delta}] \\ & - 2i\,G_\omega(\gamma_\mu)_{\alpha\beta}(\gamma^\mu)_{\gamma\delta}, \end{aligned} \tag{2}$$

where the indices label Dirac, color, and isospin.

The building blocks of mesons and baryons in the NJL model are the quark propagators. The NJL dressed quark propagator is obtained by solving the gap equation, which at the level of approximation used here is illustrated in Fig. 1

pieces in particular kinematical domains, indicating that the hadron can decay into quarks. In the version of the NJL model used here quark confinement is introduced via a particular regularization prescription which eliminates these unphysical thresholds. This regularization procedure is discussed in Sec. II.

[2]The complete SU(2) flavor NJL interaction Lagrangian can, in principle, also contain the chiral singlet terms

$$\begin{aligned} & \tfrac{1}{2}\,G_\eta[(\bar{\psi}\,\vec{\tau}\,\psi)^2 - (\bar{\psi}\,\gamma_5\,\psi)^2] - \tfrac{1}{2}\,G_f(\bar{\psi}\,\gamma^\mu\gamma_5\,\psi)^2 \\ & - \tfrac{1}{2}\,G_T[(\bar{\psi}\,i\sigma^{\mu\nu}\psi)^2 - (\bar{\psi}\,i\sigma^{\mu\nu}\vec{\tau}\,\psi)^2]. \end{aligned}$$

The complete Lagrangian explicitly breaks $U_A(1)$ symmetry unless $G_\eta = G_\pi$ and $G_T = 0$. These are the conditions imposed on the NJL Lagrangian by chiral symmetry if the chiral group is enlarged to three flavors, where the $U_A(1)$ symmetry is usually broken by introducing a 6-fermion interaction [20,22].

and reads[3]

$$iS^{-1}(k) = iS_0^{-1}(k) - \sum_{\Omega} K_\Omega\, \Omega \int \frac{d^4\ell}{(2\pi)^4}\, \mathrm{Tr}[\bar{\Omega}\, iS(\ell)], \quad (3)$$

where $S_0^{-1}(k) = \not{k} - m + i\varepsilon$ is the bare quark propagator and the trace is over Dirac, color, and isospin indices. The only piece of the $\bar{q}q$ interaction kernel given in Eq. (2) that contributes to the gap equation expressed in Eq. (3) is the isoscalar-scalar interaction $2i\, G_\pi(\mathbb{1})_{\alpha\beta}(\mathbb{1})_{\gamma\delta}$. This yields a solution of the form

$$S(k) = \frac{1}{\not{k} - M + i\varepsilon}. \quad (4)$$

The interaction kernel in the gap equation of Fig. 1 is local and therefore the dressed quark mass, M, is a constant and satisfies

$$M = m + 12\, i\, G_\pi \int \frac{d^4\ell}{(2\pi)^4}\, \mathrm{Tr}_D[S(\ell)], \quad (5)$$

where the remaining trace is over Dirac indices. For sufficiently strong coupling, $G_\pi > G_{\mathrm{critical}}$, Eq. (5) supports a nontrivial solution with $M > m$, which survives even in the chiral limit ($m = 0$).[4] This solution is a consequence of dynamical chiral symmetry breaking (DCSB) in the Nambu-Goldstone mode and it is readily demonstrated, by calculating the total energy [39], that this phase corresponds to the ground state of the vacuum.

The NJL model is a non-renormalizable quantum field theory; therefore, a regularization prescription must be specified to fully define the model. We choose the proper-time regularization scheme [38,40,41], which is introduced formally via the relation

$$\begin{aligned} \frac{1}{X^n} &= \frac{1}{(n-1)!} \int_0^\infty d\tau\, \tau^{n-1}\, e^{-\tau X}, \\ &\longrightarrow \frac{1}{(n-1)!} \int_{1/\Lambda_{\mathrm{UV}}^2}^{1/\Lambda_{\mathrm{IR}}^2} d\tau\, \tau^{n-1}\, e^{-\tau X}, \end{aligned} \quad (6)$$

where X represents a product of propagators that have been combined using Feynman parametrization. Only the ultraviolet cutoff, Λ_{UV}, is needed to render the theory finite; however, for bound states of quarks we also include the infrared cutoff, Λ_{IR}. This has the effect of eliminating unphysical thresholds for the decay of hadrons into free quarks and therefore simulates aspects of quark confinement in QCD.

Mesons in the NJL model are quark–antiquark bound states whose properties are determined by first solving the Bethe-Salpeter equation (BSE). The kernels of the gap and BSEs are intimately related, as exemplified by the vector and axial-vector Ward-Takahashi identities, which relate the quark propagator to inhomogeneous Bethe-Salpeter vertices [42]. The NJL BSE, consistent with the gap equation of Fig. 1, is illustrated in Fig. 2 and reads

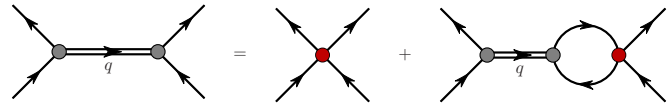

FIG. 2. (Color online) NJL Bethe-Salpeter equation for the quark-antiquark t matrix, represented as the double line with the vertices. The single line corresponds to the dressed quark propagator and the BSE $\bar{q}q$ interaction kernel, consistent with the gap equation kernel used in Eq. (5), is given by Eq. (2).

$$\mathcal{T}(q) = \mathcal{K} + \int \frac{d^4k}{(2\pi)^4}\, \mathcal{K}\, S(k+q)\, S(k)\, \mathcal{T}(q), \quad (7)$$

where q is the total momentum of the two-body system, $\mathcal{T}$ is the two-body t matrix, and $\mathcal{K}$ is the $\bar{q}q$ interaction kernel given in Eq. (2). Dirac, color and isospin indices have been suppressed in Eq. (7). Solutions to the BSE in the $\bar{q}q$ channels with quantum numbers that correspond to those of the pion,[5] ρ, and ω have the forms

$$\mathcal{T}_\pi(q)_{\alpha\beta,\gamma\delta} = (\gamma_5\tau_i)_{\alpha\beta}\ \ \tau_\pi(q)\, (\gamma_5\tau_i)_{\gamma\delta}, \quad (8)$$

$$\mathcal{T}_\rho(q)_{\alpha\beta,\gamma\delta} = (\gamma_\mu\tau_i)_{\alpha\beta}\ \ \tau_\rho^{\mu\nu}(q)\, (\gamma_\nu\tau_i)_{\gamma\delta}, \quad (9)$$

$$\mathcal{T}_\omega(q)_{\alpha\beta,\gamma\delta} = (\gamma_\mu)_{\alpha\beta}\ \ \tau_\omega^{\mu\nu}(q)\, (\gamma_\nu)_{\gamma\delta}, \quad (10)$$

where τ_i are the Pauli matrices and

$$\tau_\pi(q) = \frac{-2i\, G_\pi}{1 + 2\, G_\pi\, \Pi_{PP}(q^2)}, \quad (11)$$

$$\tau_\rho^{\mu\nu}(q) = \frac{-2i\, G_\rho}{1 + 2\, G_\rho\, \Pi_{VV}(q^2)} \left[g^{\mu\nu} + 2\, G_\rho\, \Pi_{VV}(q^2)\, \frac{q^\mu q^\nu}{q^2} \right], \quad (12)$$

$$\tau_\omega^{\mu\nu}(q) = \frac{-2i\, G_\omega}{1 + 2\, G_\omega\, \Pi_{VV}(q^2)} \left[g^{\mu\nu} + 2\, G_\omega\, \Pi_{VV}(q^2) \frac{q^\mu q^\nu}{q^2} \right]. \quad (13)$$

The functions $\tau_\pi(q)$, $\tau_\rho^{\mu\nu}(q)$, and $\tau_\omega^{\mu\nu}(q)$ are the reduced t matrices, which are interpreted as propagators for the pion, ρ, and ω mesons. The bubble diagrams in Eqs. (11)–(13) have

[3] In principle, there is an infinite tower of higher-order terms that can appear in the NJL gap equation kernel, with meson loops an important example. However, in keeping with the standard treatment, these higher-order terms are not included. We do, however, include a single pion loop as a perturbative correction to the quark-photon vertex. This is discussed in Sec. IV.

[4] In the proper-time regularization scheme defined in Eq. (6) the critical coupling in the chiral limit has the value $G_{\mathrm{critial}} = \frac{\pi^2}{3}(\Lambda_{\mathrm{UV}}^2 - \Lambda_{\mathrm{IR}}^2)^{-1}$.

[5] The NJL Lagrangian of Eq. (1) implies that the $G_\rho(\bar{\psi}\, \gamma^\mu\gamma_5\vec{\tau}\, \psi)^2$ $\bar{q}q$ interaction should also contribute in the pionic channel, giving rise to π-a_1 mixing. However, because the a_1 meson is much heavier than the pion, the amount of mixing is small and we therefore ignore π-a_1 mixing in this work.

the form

$$\Pi_{PP}(q^2)\delta_{ij} = 3i\int \frac{d^4k}{(2\pi)^4}\,\mathrm{Tr}[\gamma_5\,\tau_i\,S(k)\,\gamma_5\,\tau_j\,S(k+q)], \tag{14}$$

$$\Pi_{VV}(q^2)\left(g^{\mu\nu}-\frac{q^\mu q^\nu}{q^2}\right)\delta_{ij} = 3i\int \frac{d^4k}{(2\pi)^4}\,\mathrm{Tr}[\gamma^\mu\tau_i\,S(k)\,\gamma^\nu\tau_j\,S(k+q)], \tag{15}$$

where the traces are over Dirac and isospin indices. Meson masses are then defined by the pole in the corresponding two-body t matrix.

In a covariant formulation a two-body t matrix, near a bound-state pole of mass m_i, behaves as

$$\mathcal{T}(q) \to \frac{\Gamma_i(q)\,\overline{\Gamma}_i(q)}{q^2-m_i^2}, \tag{16}$$

where $\Gamma_i(q)$ is the normalized homogeneous Bethe-Salpeter vertex function for the bound state. Expanding the t matrices in Eqs. (8)–(10) about the pole masses gives

$$\Gamma_\pi^i = \sqrt{Z_\pi}\,\gamma_5\,\tau_i, \quad \Gamma_\rho^{\mu,i} = \sqrt{Z_\rho}\,\gamma^\mu\,\tau_i, \quad \Gamma_\omega^\mu = \sqrt{Z_\omega}\,\gamma^\mu, \tag{17}$$

where i is an isospin index and the normalization factors are given by

$$Z_\pi^{-1} = -\frac{\partial}{\partial q^2}\,\Pi_{PP}(q^2)\Big|_{q^2=m_\pi^2}, \tag{18}$$

$$Z_{\rho,\omega}^{-1} = -\frac{\partial}{\partial q^2}\,\Pi_{VV}(q^2)\Big|_{q^2=m_{\rho,\omega}^2}. \tag{19}$$

These residues are interpreted as the effective meson-quark-quark coupling constants. Homogeneous Bethe-Salpeter vertex functions are an essential ingredient in, for example, triangle diagrams that determine the meson form factors.

Baryons in the NJL model are naturally described as bound states of three dressed quarks. The properties of these bound states are determined by the relativistic Faddeev equation whose solution gives the Poincaré covariant Faddeev amplitude. To construct the interaction kernel of the Faddeev equation we require the elementary quark-quark interaction kernel. Using Fierz transformations to rewrite Eq. (1) as a sum of qq interactions, keeping only the isoscalar-scalar ($0^+, T=0$) and isovector–axial-vector ($1^+, T=1$) two-body channels, the NJL interaction Lagrangian takes the form

$$\mathcal{L}_{I,qq} = G_s[\bar\psi\,\gamma_5\,C\,\tau_2\,\beta_A\,\bar\psi^T][\psi^T\,C^{-1}\gamma_5\,\tau_2\,\beta_A\,\psi] + G_a[\bar\psi\,\gamma_\mu\,C\,\tau_i\tau_2\,\beta_A\,\bar\psi^T][\psi^T\,C^{-1}\gamma^\mu\,\tau_2\tau_i\,\beta_A\,\psi], \tag{20}$$

where $C = i\gamma_2\gamma_0$ is the charge conjugation matrix and the couplings G_s and G_a give the strength of the scalar and axial-vector qq interactions. Because only color $\bar 3$ qq states can couple to a third quark to form a colorless 3-quark state, we must have $\beta_A = \sqrt{\frac{3}{2}}\,\lambda_A (A = 2,5,7)$ [28]. The Lagrangian of Eq. (20) gives an elementary qq interaction kernel,

$$\mathcal{K}_{\alpha\beta,\gamma\delta} = 4i\,G_s(\gamma_5\,C\,\tau_2\,\beta_A)_{\alpha\beta}(C^{-1}\,\gamma_5\,\tau_2\,\beta_A)_{\gamma\delta} + 4i\,G_a(\gamma_\mu\,C\,\tau_i\tau_2\,\beta_A)_{\alpha\beta}(C^{-1}\,\gamma^\mu\,\tau_2\tau_i\,\beta_A)_{\gamma\delta}. \tag{21}$$

This kernel has been truncated to support only scalar and axial-vector diquark correlations because the pseudoscalar and vector diquark components of the nucleon must predominantly be in $\ell = 1$ states and are therefore suppressed. Pseudoscalar and vector diquarks are also usually found to be considerably heavier than their scalar and axial-vector counterparts [43].

Using Eq. (21) as the interaction kernel in the Faddeev equation allows us to first sum all two-body qq interactions to form the scalar and axial-vector diquark t matrices. Diquark correlations in the nucleon are therefore a natural consequence of the strong coupling in the color $\bar 3$ quark-quark interaction channel. The BSE in the qq channel for our NJL model reads

$$\mathcal{T}(q) = \mathcal{K} + \frac{1}{2}\int \frac{d^4k}{(2\pi)^4}\,\mathcal{K}\,S(k+q)\,S(-k)\,\mathcal{T}(q), \tag{22}$$

where $\mathcal{K}$ is given in Eq. (21) and there is a symmetry factor of $\frac{1}{2}$ relative to the $\bar qq$ BSE of Eq. (7). The solutions to the BSE in the scalar and axial-vector diquark channels are

$$\mathcal{T}_s(q)_{\alpha\beta,\gamma\delta} = (\gamma_5\,C\,\tau_2\,\beta_A)_{\alpha\beta}\tau_s(q)(C^{-1}\gamma_5\,\tau_2\,\beta_A)_{\gamma\delta}, \tag{23}$$

$$\mathcal{T}_a(q)_{\alpha\beta,\gamma\delta} = (\gamma_\mu\,C\,\tau_i\tau_2\,\beta_A)_{\alpha\beta}\tau_a^{\mu\nu}(q)(C^{-1}\gamma_\nu\,\tau_2\tau_i\,\beta_A)_{\gamma\delta}, \tag{24}$$

where

$$\tau_s(q) = \frac{-4i\,G_s}{1+2\,G_s\,\Pi_{PP}(q^2)}, \tag{25}$$

$$\tau_a^{\mu\nu}(q) = \frac{-4i\,G_a}{1+2\,G_a\,\Pi_{VV}(q^2)}\left[g^{\mu\nu}+2\,G_a\,\Pi_{VV}(q^2)\,\frac{q^\mu q^\nu}{q^2}\right]. \tag{26}$$

The scalar and axial-vector diquark masses are defined as the poles[6] in Eqs. (25) and (26), respectively, and the homogeneous Bethe-Salpeter vertices read

$$\Gamma_s = \sqrt{Z_s}\,\gamma_5\,C\,\tau_2\,\beta_A, \quad \Gamma_a^{\mu,i} = \sqrt{Z_a}\,\gamma^\mu\,C\,\tau_i\,\tau_2\,\beta_A, \tag{27}$$

where i is an isospin index. The pole residues are given by

$$Z_s^{-1} = -\frac{1}{2}\,\frac{\partial}{\partial q^2}\,\Pi_{PP}(q^2)\Big|_{q^2=M_s^2}, \tag{28}$$

$$Z_a^{-1} = -\frac{1}{2}\,\frac{\partial}{\partial q^2}\,\Pi_{VV}(q^2)\Big|_{q^2=M_a^2}, \tag{29}$$

where M_s and M_a are the scalar and axial-vector diquark masses. These pole residues are interpreted as the effective diquark-quark-quark couplings.

[6]In QCD these poles should not exist, because diquarks, as colored objects, are not part of the physical spectrum. Nevertheless, diquark states play a very important role in many phenomenological studies, for example, in the spin and flavor dependence of nucleon PDFs [44,45]. They have also been observed in lattice QCD studies [46] as well as model studies of QCD, for example, in the rainbow-ladder truncation of the Dyson-Schwinger equations (DSEs). In the DSE approach diagrams beyond the rainbow-ladder truncation have been shown to remove the pole in the diquark t matrix [47].

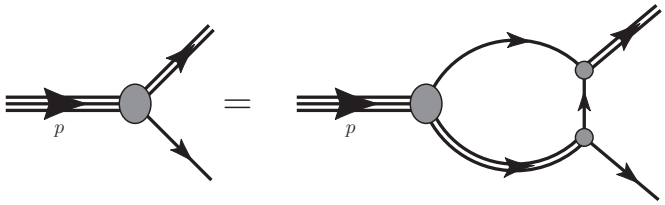

FIG. 3. Homogeneous Faddeev equation for the nucleon in the NJL model. The single lines represent the quark propagator and the double lines the diquark propagators. Both scalar and axial-vector diquarks are included in these calculations.

The homogeneous Faddeev equation is illustrated in Fig. 3, where diquark correlations have been made explicit. The relativistic Faddeev equation in the NJL model has been solved numerically in Refs. [48–50], where the integrals were regularized using the Lepage-Brodsky and transverse momentum cutoff schemes. In the proper-time regularization scheme used here, solving the Faddeev equation is much more challenging and we therefore employ the static approximation to the quark exchange kernel. In this approximation the propagator of the exchanged quark becomes $S(k) \to -\frac{1}{M}$ [48]. The nucleon vertex function then takes the form

$$\Gamma_N(p) = \sqrt{-Z_N}\,\Gamma = \sqrt{-Z_N}\begin{bmatrix}\Gamma_s(p)\\ \Gamma_a^{\mu,i}(p)\end{bmatrix} = \sqrt{-Z_N}\begin{bmatrix}\alpha_1 \\ \left(\alpha_2\,\frac{p^\mu}{M_N}\,\gamma_5 \;+\alpha_3\,\gamma^\mu\gamma_5\right)\frac{\tau_i}{\sqrt{3}}\end{bmatrix}\chi(t)\,u(p), \tag{30}$$

where i is an isospin index and $\chi_N(t)$ is the nucleon isospinor:

$$\chi\left(\tfrac{1}{2}\right) = \begin{pmatrix}1\\0\end{pmatrix}, \quad \chi\left(-\tfrac{1}{2}\right) = \begin{pmatrix}0\\1\end{pmatrix}. \tag{31}$$

The first element in the column vector of Eq. (30) represents the piece of the nucleon vertex function consisting of a quark and a scalar diquark, while the second element represents the quark and axial-vector diquark component. The nucleon mass is labeled by M_N and the Dirac spinor is normalized such that $\bar{u}_N\,u_N = 1$. Z_N is the nucleon vertex function normalization and α_1,α_2,α_3 are obtained by solving the Faddeev equation. After projection onto positive parity, spin-$\frac{1}{2}$ and isospin-$\frac{1}{2}$, the homogeneous Faddeev equation is given by [28]

$$\Gamma_N(p,s) = K(p)\,\Gamma_N(p,s), \tag{32}$$

which in matrix form reads

$$\begin{bmatrix}\Gamma_s\\ \Gamma_a^\mu\end{bmatrix} = \frac{3}{M}\begin{bmatrix}\Pi_{Ns} & \sqrt{3}\gamma_\alpha\gamma_5\,\Pi_{Na}^{\alpha\beta}\\ \sqrt{3}\gamma_5\gamma^\mu\,\Pi_{Ns} & -\gamma_\alpha\gamma^\mu\,\Pi_{Na}^{\alpha\beta}\end{bmatrix}\begin{bmatrix}\Gamma_s\\ \Gamma_{a,\beta}\end{bmatrix}. \tag{33}$$

The quark-diquark bubble diagrams are defined as

$$\Pi_{Ns}(p) = \int\frac{d^4k}{(2\pi)^4}\,\tau_s(p-k)\,S(k), \tag{34}$$

$$\Pi_{Na}^{\mu\nu}(p) = \int\frac{d^4k}{(2\pi)^4}\,\tau_a^{\mu\nu}(p-k)\,S(k). \tag{35}$$

TABLE I. Model parameters constrained to reproduce the physical pion, ρ, and ω masses; the pion decay constant; and the nucleon and Δ baryon masses. The infrared regulator and the dressed quark mass are assigned their values *a priori*. The regularization parameters and dressed quark mass are in units of GeV, while the couplings are in units of GeV $^{-2}$.

$\Lambda_{\rm IR}$	$\Lambda_{\rm UV}$	M	G_π	G_ρ	G_ω	G_s	G_a
0.240	0.645	0.4	19.0	11.0	10.4	5.8	4.9

The vertex normalization of Eq. (30) is given by

$$Z_N = \left[\overline{\Gamma}\,\frac{\partial\,\Pi_N(p)}{\partial p^2}\,\Gamma\right]^{-1}_{p^2=M_N^2}, \tag{36}$$

where

$$\Pi_N(p) = \begin{bmatrix}\Pi_{Ns}(p) & 0\\ 0 & \Pi_{Na}^{\alpha\beta}(p)\end{bmatrix}. \tag{37}$$

Regulating expressions such as those in Eqs. (34) and (35) using the proper-time scheme is tedious. Therefore, to render the Faddeev equation and form-factor calculations tractable we make the pole approximation to the meson and diquark t matrices; for example, Eqs. (25) and (26) become

$$\tau_s(q) \to -\frac{i\,Z_s}{q^2 - M_s^2 + i\,\varepsilon}, \tag{38}$$

$$\tau_a^{\mu\nu}(q) \to -\frac{i\,Z_a}{q^2 - M_a^2 + i\,\varepsilon}\left(g^{\mu\nu} - \frac{q^\mu q^\nu}{M_a^2}\right). \tag{39}$$

Similar expressions are obtained in the meson sector.

In summary, the model parameters consist of the two regularization scales $\Lambda_{\rm IR}$ and $\Lambda_{\rm UV}$, the dressed quark mass M,[7] and the Lagrangian coupling constants G_π, G_ρ, G_ω, G_s, G_a. The infrared regularization scale is associated with confinement and therefore should be of the order $\Lambda_{\rm QCD}$, and we choose $\Lambda_{\rm IR} = 0.240$ GeV and for the constituent quark mass take $M = 0.4$ GeV. The physical pion mass ($m_\pi = 140$ MeV) and decay constant ($f_\pi = 92$ MeV) determine $\Lambda_{\rm UV}$ and G_π. The physical masses of the ρ ($m_\rho = 770$ MeV) and ω ($m_\omega = 782$ MeV) mesons constrain G_ρ and G_ω, respectively, while the physical nucleon ($M_N = 940$ MeV) and Δ ($M_\Delta = 1232$ MeV) baryon masses determine G_s and G_a.[8] Numerical values are given in Table I.

Using the parameters given in Table I, we obtain the following results for the residues of the two-body t matrices: $Z_\pi = 17.9$, $Z_\rho = 6.96$, $Z_\omega = 6.63$, $Z_s = 11.1$, and $Z_a = 6.73$. For the nucleon vertex function of Eq. (30) we find $Z_N = 28.1$ and $(\alpha_1, \alpha_2, \alpha_3) = (0.55, 0.05, -0.40)$, where the scalar and axial-vector diquark masses are $M_s = 0.768$ GeV and $M_a = 0.929$ GeV.

[7] Alternatively, one could specify a current quark mass, as one determines the other through the gap equation.

[8] The relativistic Faddeev equation for the Δ baryon is discussed, for example, in Ref. [28].

III. NUCLEON ELECTROMAGNETIC CURRENT

The electromagnetic current of an on-shell nucleon, expressed in terms of the Dirac and Pauli form factors, has the form

$$j^{\mu}_{\lambda'\lambda}(p',p) = \langle p',\lambda'|J^{\mu}_{\rm em}|p,\lambda\rangle = u(p',\lambda')\left[\gamma^{\mu}\,F_1(Q^2)+\frac{i\sigma^{\mu\nu}q_{\nu}}{2\,M_N}\,F_2(Q^2)\right]u(p,\lambda), \tag{40}$$

where $q = p' - p$ is the 4-momentum transfer, $Q^2 \equiv -q^2$, and λ, λ' represent the initial and final nucleon helicity, respectively. The nucleon's electric and magnetic Sachs form factors [51], which diagonalize the Rosenbluth cross section, are then given by

$$G_E(Q^2) = F_1(Q^2) - \frac{Q^2}{4\,M_N^2}\,F_2(Q^2), \tag{41}$$

$$G_M(Q^2) = F_1(Q^2) + F_2(Q^2). \tag{42}$$

Hadron form factors can be decomposed into a sum over the quark charges multiplied by quark-sector form factors, such that

$$F_h(Q^2) = \sum_q e_q\,F_h^q(Q^2). \tag{43}$$

The quark-sector form factors $F_h^q(Q^2)$ represent the contribution of the current quarks of flavor q to the total hadron form factor $F_h(Q^2)$. The proton and neutron form factors expressed in terms of quark-sector form factors read

$$F_{ip}(Q^2) = e_u\,F_{ip}^u(Q^2) + e_d\,F_{ip}^d(Q^2) + \cdots, \tag{44}$$

$$F_{in}(Q^2) = e_u\,F_{in}^u(Q^2) + e_d\,F_{in}^d(Q^2) + \cdots, \tag{45}$$

where $i = 1, 2$. Note that in light of the experimental discovery that the strange quarks contribute very little to the nucleon electromagnetic form factors [52–55], we neglect their contribution to Eqs. (44) and (45). Assuming equal u and d current quark masses and neglecting electroweak corrections, the u and d quark-sector form factors of the nucleon must satisfy the charge symmetry constraints:

$$F_{in}^d(Q^2) = F_{ip}^u(Q^2) \quad \text{and} \quad F_{in}^u(Q^2) = F_{ip}^d(Q^2). \tag{46}$$

Experimentally, if electroweak and heavy quark effects are small, the u and d quark-sector form factors are given accurately by

$$F_{ip}^u = 2\,F_{ip} + F_{in}, \quad F_{ip}^d = F_{ip} + 2\,F_{in}. \tag{47}$$

Recent accurate data for the neutron form factors has enabled a precise determination of the quark-sector proton form factors [56]. We discuss results for these quark-sector form factors in Sec. VI.

The slope of an electromagnetic form factor at $Q^2 = 0$ is a measure of either the squared rms charge or magnetic radius of a hadron. Unless stated otherwise, all squared rms radii are defined by

$$\langle r^2\rangle = -\frac{6}{\eta}\,\frac{\partial\,f(Q^2)}{\partial\,Q^2}\bigg|_{Q^2=0} \quad \Big|\quad \eta = \begin{cases} 1 & \text{if} \quad f(0) = 0, \\ f(0) & \text{if} \quad f(0) \neq 0, \end{cases} \tag{48}$$

where $f(Q^2)$ is an arbitrary form factor. This definition reproduces the standard nucleon results for the charge and magnetic radii defined by the Sachs form factors,

$$\langle r_E^2\rangle = -6\,\frac{\partial\,G_E(Q^2)}{\partial\,Q^2}\bigg|_{Q^2=0}, \tag{49}$$

$$\langle r_M^2\rangle = -\frac{6}{G_M(0)}\,\frac{\partial\,G_M(Q^2)}{\partial\,Q^2}\bigg|_{Q^2=0}, \tag{50}$$

but also generalizes to radii defined with respect to the Dirac and Pauli form factors and quark-sector form factors. Hadronic radii, in units of fm, are obtained from the result of Eq. (48) using

$$r \equiv \text{sign}(\langle r^2\rangle)\,\sqrt{|\langle r^2\rangle|}. \tag{51}$$

To calculate the nucleon electromagnetic current and therefore the Dirac and Pauli form factors, one must know the manner in which the nucleon described in Sec. II couples to the photon, guaranteeing electromagnetic gauge invariance. The necessary Feynman diagrams are illustrated in Fig. 4 and a proof of gauge invariance is given in Appendix B. We include both scalar and axial-vector diquarks in our nucleon wave function and therefore the diagrams in Fig. 4 represent six distinct Feynman diagrams. The diagram on the left, referred to as the *quark diagram*, represents the processes where the photon couples to a dressed quark with either a scalar or an axial-vector diquark as a spectator. The *diquark diagram*, on the right in Fig. 4, represents four Feynman diagrams; the photon can couple to a scalar diquark, an axial-vector diquark or cause a transition between these two diquark states. Importantly, in the *diquark diagram* the photon couples to the quarks inside each diquark, thereby resolving internal diquark structure and resulting in, for example, diquarks with a finite size. In principle, for the diquark diagram, the photon should couple to an off-shell diquark; however, in this work we limit the Lorentz structure of the photon-diquark interaction to that of an on-shell diquark. In general, such an on-shell approximation for a vertex function can only be formulated if it appears between pole parts of two Green's functions [57],

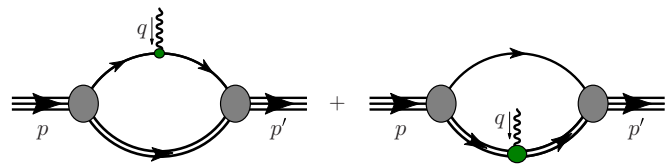

FIG. 4. (Color online) Feynman diagrams representing the nucleon electromagnetic current. The diagram on the left is called the *quark diagram* and the diagram on the right the *diquark diagram*. In the diquark diagram the photon interacts with each quark inside the nonpointlike diquark.

which, in this work, is consistent with the pole approximations for the diquark t matrices described in Eqs. (38) and (39).

The coupling of a photon to a dressed quark and to on-shell diquarks is discussed in Secs. IV and V.

IV. QUARK-PHOTON VERTEX

The quark-photon vertex in the NJL model, and other field theoretic approaches, is given by the solution to an inhomogeneous BSE. The NJL model version of this equation, consistent with the truncation used in the gap and BSEs discussed Sec. II, is represented diagrammatically in Fig. 5. The large oval represents the quark-photon vertex, $\Lambda^{\mu}_{\gamma Q}(p',p)$, the 4-fermion interaction kernel is given in Eq. (2) and the elementary vertex, which gives the inhomogeneous driving term, has the form $\gamma^{\mu}\,\hat{Q}$ (where $\hat{Q}$ is the quark charge operator). The second equality in Fig. 5 expresses this equation in an equivalent form using the $\bar{q}q$ t matrices.

The quark charge operator is

$$\hat{Q} = \begin{pmatrix} e_u & 0 \\ 0 & e_d \end{pmatrix} = \frac{1}{6} + \frac{\tau_3}{2}, \tag{52}$$

where $e_u = \frac{2}{3}$ and $e_d = -\frac{1}{3}$ are the u and d quark charges. The quark-photon vertex therefore has both an isoscalar and an isovector component, which may, in general, be expressed in the form

$$\Lambda^{\mu}_{\gamma Q}(p',p) = \frac{1}{6}\,\Lambda^{\mu}_{\omega}(p',p) + \frac{\tau_3}{2}\,\Lambda^{\mu}_{\rho}(p',p). \tag{53}$$

The quark-photon vertex, separated into flavor sectors defined by the dressed quarks, reads

$$\Lambda^{\mu}_{\gamma Q}(p',p) = \Lambda^{\mu}_{U}(p',p)\,\frac{1+\tau_3}{2} + \Lambda^{\mu}_{D}(p',p)\,\frac{1-\tau_3}{2}. \tag{54}$$

In general, each dressed quark component of the quark-photon vertex contains contributions from both the u and d current quarks. This will prove important when we consider quark-sector form factors and associated charge symmetry constraints. Note that throughout this paper we use a capital $Q = (U, D)$ to indicate that an object is associated with dressed quarks and a lowercase $q = (u, d)$ to represent the current quarks of the NJL and QCD Lagrangians.

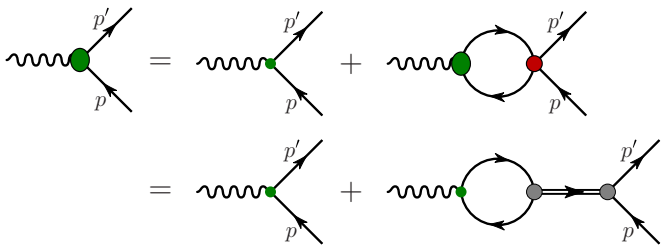

FIG. 5. (Color online) Inhomogeneous BSE whose solution gives the quark-photon vertex, represented as the large shaded oval. The small dot is the inhomogeneous driving term, while the shaded circle is the $\bar{q}q$ interaction kernel given in Eq. (2). Only the ρ and ω interaction channels contribute. This integral equation can equivalently be represented using the elementary quark-photon interaction and the ρ and ω t matrices, given in Eqs. (12) and (13). This case is depicted by the second equality.

The quark-photon vertex has in general 12 Lorentz structures [58], 4 longitudinal and 8 pieces transverse to the photon momentum, where each Lorentz structure is accompanied by a scalar function of the three variables q^2, p'^2, and p^2.[9] The standard NJL $\bar{q}q$ interaction kernel, as employed in Sec. II for the gap and BSE equations, is momentum independent, which implies that the quark-photon vertex can only depend on the momentum transfer $q = p' - p$, not p' and p separately. Therefore, in this work, the contributions to the vertex functions of Eq. (53) from the NJL BSE, take the form

$$\Lambda^{(\mathrm{bse})\mu}_{\omega}(q) = \gamma^{\mu} + \left(\gamma^{\mu} - \frac{q^{\mu}\not{q}}{q^2}\right)\hat{F}_{1\omega}(q^2) + \frac{i\sigma^{\mu\nu}q_{\nu}}{2\,M}F_{2\omega}(q^2), \tag{55}$$

$$\Lambda^{(\mathrm{bse})\mu}_{\rho}(q) = \gamma^{\mu} + \left(\gamma^{\mu} - \frac{q^{\mu}\not{q}}{q^2}\right)\hat{F}_{1\rho}(q^2) + \frac{i\sigma^{\mu\nu}q_{\nu}}{2\,M}F_{2\rho}(q^2). \tag{56}$$

With the quark propagator of Eq. (4), these results satisfy the Ward-Takahashi identity,

$$q_{\mu}\,\Lambda^{\mu}_{\gamma Q}(p',p) = \hat{Q}[S^{-1}(p') - S^{-1}(p)], \tag{57}$$

demanded by U(1) vector gauge invariance.

Current conservation at the hadron level implies that the $q^{\mu}\not{q}/q^2$ term in Eqs. (55) and (56) cannot contribute to hadron form factors. We therefore write our effective vertex as

$$\Lambda^{(\mathrm{bse})\mu}_{i}(q) = \gamma^{\mu}\,F_{1i}(q^2) + \frac{i\sigma^{\mu\nu}q_{\nu}}{2\,M}\,F_{2i}(q^2), \tag{58}$$

where $i = (\omega, \rho)$ and $F_{1i}(q^2) = 1 + \hat{F}_{1i}(q^2)$. This vertex has the same form as the electromagnetic current for an on-shell spin-$\frac{1}{2}$ fermion. For a pointlike quark $F_{1\omega}(q^2) = 1 = F_{1\rho}(q^2)$ and $F_{2\omega}(q^2) = 0 = F_{2\rho}(q^2)$. However, interactions in the NJL model not only dynamically generate a dressed quark mass but also generate nontrivial dressed quark form factors.

The inhomogeneous BSE for the quark-photon vertex, depicted in Fig. 5, has the form

$$\Lambda^{\mu}_{\gamma Q}(p',p) = \gamma^{\mu}\left(\frac{1}{6} + \frac{\tau_3}{2}\right) + \sum_{\Omega} K_{\Omega}\;\Omega \times i\int\frac{d^4k}{(2\pi)^4}\,\mathrm{Tr}[\bar{\Omega}\,S(k+q)\,\Lambda^{\mu}_{\gamma Q}(p',p)\,S(k)], \tag{59}$$

where $\sum_{\Omega} K_{\Omega}\;\Omega_{\alpha\beta}\,\bar{\Omega}_{\lambda\varepsilon}$ represents the interaction kernel given in Eq. (2). The Dirac and isospin structure of $\Lambda^{\mu}_{\gamma Q}(p',p)$, given in Eqs. (53), (55), and (56), implies that of the interaction channels in Eq. (2) only the isovector-vector, $-2i\,G_{\rho}(\gamma_{\mu}\vec{\tau})_{\alpha\beta}(\gamma^{\mu}\vec{\tau})_{\gamma\delta}$, and isoscalar-vector, $-2i\,G_{\omega}(\gamma_{\mu})_{\alpha\beta}(\gamma^{\mu})_{\gamma\delta}$, pieces can contribute.

[9] The 12 Lorentz structures in the quark-photon vertex are not all independent, because, for example, the Ward-Takahashi identity and time-reversal invariance place additional constraints.

The dressed quark form factors obtained from the inhomogeneous BSE, associated with the electromagnetic current of Eq. (58), are

$$F_{1i}(q^2) = \frac{1}{1 + 2\,G_i\,\Pi_{VV}(q^2)}, \quad F_{2i}(q^2) = 0, \tag{60}$$

where $i = \omega, \rho$. Comparison with Eqs. (12) and (13) indicate that $F_{1\omega}$ and $F_{1\rho}$ have a pole at $q^2 = m_\omega^2$ and m_ρ^2, respectively. The NJL BSE kernel of Eq. (2) does not generate Pauli form factors for the dressed quarks because it does not include the tensor-tensor 4-fermion interaction. The dressed-up and dressed-down quark form factors given by the BSE therefore read

$$F_{1Q}^{(\mathrm{bse})}(Q^2) = \tfrac{1}{6}\,F_{1\omega}(Q^2) \pm \tfrac{1}{2}\,F_{1\rho}(Q^2), \tag{61}$$

where the plus sign is associated with a dressed-up quark. The superscript (bse) indicates that these form factors are obtained solely from the BSE.

Results for the dressed quark BSE form factors are illustrated as the dashed lines in Figs. 6. A notable feature of these results is that they do not drop to zero as $Q^2 \to \infty$,

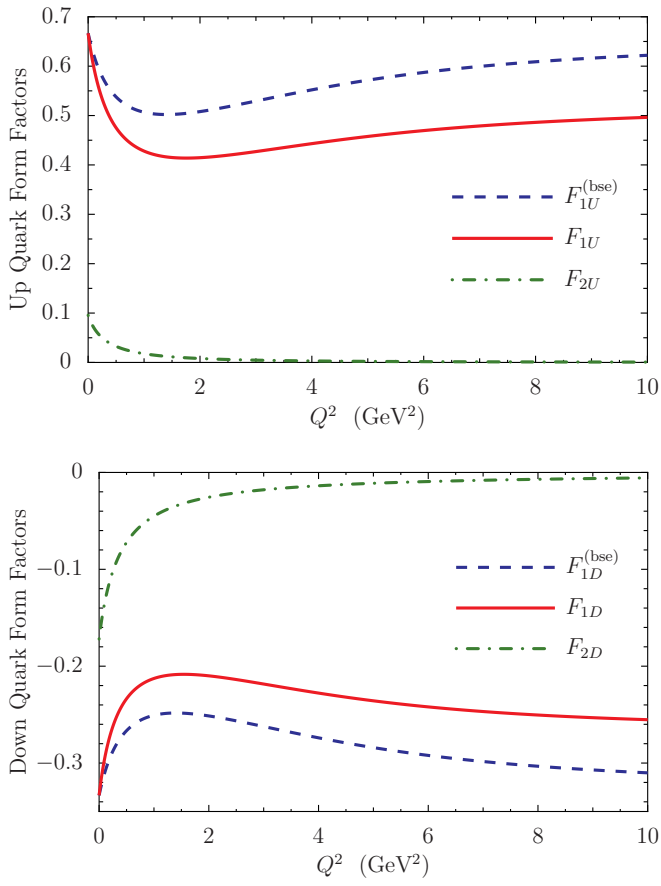

FIG. 6. (Color online) (Top) Dressed-up quark form factors. The dashed line is the Dirac form factor obtained from the BSE of Eq. (59); the solid and dash-dotted lines are, respectively, the Dirac and Pauli form factors generated by also including the pion loop corrections illustrated in Fig. 8. (Bottom) Dressed-down quark form factors. Each curve represents an analogous form factor to those in the top panel.

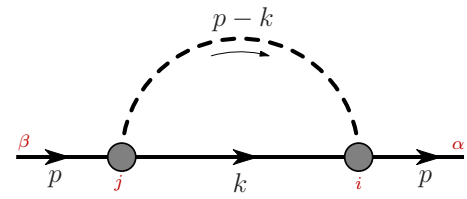

FIG. 7. (Color online) Pion loop contribution to the dressed quark self-energy. The pion couples to the dressed quark via $\gamma_5\,\tau_i$ and the pion t matrix is approximated by its pole form.

but instead behave as

$$F_{1U}^{(\mathrm{bse})}(Q^2) \overset{Q^2\to\infty}{=} e_u, \quad F_{1D}^{(\mathrm{bse})}(Q^2) \overset{Q^2\to\infty}{=} e_d, \tag{62}$$

signifying that at infinite Q^2 the photon interacts with a bare current quark. This result is consistent with QCD expectations based on asymptotic freedom.

Pion loop corrections to the quark-photon vertex are also considered and treated as a perturbation to the dressed quark form factors obtained from the BSE, as given in Eqs. (60) and (61). In this case the dressed quark propagator receives an additional self-energy correction which is illustrated in Fig. 7.[10] In addition to the pionic self-energies on the dressed quarks, pion exchange between quarks should also be included in the two-body kernels that enter the Bethe-Salpeter and Faddeev equations. However, it is straightforward to show that in the limit where the nucleon and Δ are mass degenerate, including only self-energy correction on the dressed quarks yields essentially the correct leading nonanalytic behavior of the electromagnetic form factors as a function of quark mass. Further, in form-factor calculations diagrams with a photon coupling to an exchanged pion do not contribute because of the cancellation between π^+ and π^- exchange. This self-energy is evaluated using a pole approximation, where the external quark is assumed on mass shell. The pion loop therefore shifts the dressed quark mass by a constant, giving a quark propagator of the form

$$\tilde{S}(k) = Z\,S(k), \qquad Z = 1 + \left.\frac{\partial\,\Sigma(p)}{\partial \not{p}}\right|_{\not{p}=M}, \tag{63}$$

where $S(k)$ is the usual Feynman propagator for a dressed quark of mass[11] M and the self-energy

[10] Chiral symmetry as expressed in the the NJL Lagrangian of Eq. (1) demands that the σ meson be included also; however, because the σ has charge zero and (in this work) $m_\pi/m_\sigma \simeq 0.18$, these additional correction are small and are not included.

[11] When including pion loops on the dressed quarks we renormalize the G_π coupling in the NJL Lagrangian to keep the dressed quark mass fixed.

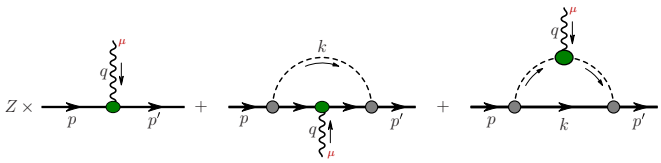

FIG. 8. (Color online) Pion loop contributions to the quark-photon vertex. The quark wave function renormalization factor Z represents the probability of striking a dressed quark without a pion cloud. In the first two diagrams the photon couples to the dressed quark with a vertex of the general form given by Eq. (53) and defined by Eqs. (58) and (60). The shaded oval in the third diagram represents the quark-pion vertex, which we approximate by its pole form. It is therefore given by $(\ell' + \ell)F_\pi(Q^2)$, where $F_\pi(Q^2)$ is the usual pion form factor [see Eq. (86) and associated discussion].

reads[12]

$$\Sigma(p) = -\int \frac{d^4k}{(2\pi)^2}\, \gamma_5\, \tau_i\, S(p-k)\, \gamma_5\, \tau_i\, \tau_\pi(k). \tag{64}$$

When evaluating $\Sigma(p)$ the reduced pion t matrix is approximated by its pole form; that is,

$$\tau_\pi(k) \to \frac{i\, Z_\pi}{k^2 - m_\pi^2 + i\varepsilon}. \tag{65}$$

The quark wave function renormalization factor, Z, represents the probability to strike a dressed quark without the pion cloud and is essential to maintain charge conservation. Using the parameters in Table I gives $Z = 0.80$.

The quark electromagnetic current, including pion loops, is illustrated in Fig. 8. Evaluating this current between on-shell constituent quarks, gives for the dressed quark-sector currents of Eq. (54),

$$\Lambda_Q^\mu(p',p) = \gamma^\mu\, F_{1Q}(Q^2) + \frac{i\sigma^{\mu\nu}q_\nu}{2\,M}\, F_{2Q}(Q^2), \tag{66}$$

where $Q = (U, D)$. The dressed quark form factors read

$$F_{1U} = Z\big[\tfrac{1}{6}\, F_{1\omega} + \tfrac{1}{2}\, F_{1\rho}\big] + [F_{1\omega} - F_{1\rho}]f_1^{(q)} + F_{1\rho}\, f_1^{(\pi)}, \tag{67}$$

$$F_{1D} = Z\big[\tfrac{1}{6}\, F_{1\omega} - \tfrac{1}{2}\, F_{1\rho}\big] + [F_{1\omega} + F_{1\rho}]f_1^{(q)} - F_{1\rho}\, f_1^{(\pi)}, \tag{68}$$

$$F_{2U} = [F_{1\omega} - F_{1\rho}]f_2^{(q)} + F_{1\rho}\, f_2^{(\pi)}, \tag{69}$$

$$F_{2D} = [F_{1\omega} + F_{1\rho}]f_2^{(q)} - F_{1\rho}\, f_2^{(\pi)}, \tag{70}$$

where the Q^2 dependence of each form factor has been omitted. The body form factors, $f_1^{(q)}$ and $f_2^{(q)}$, originate from the second diagram in Fig. 8, while $f_1^{(\pi)}$ and $f_2^{(\pi)}$ are the body form factors from the third diagram, which also contain the pion body form factor [see discussion associated with Eq. (86)]. These body form factors are illustrated in Fig. 9. When evaluating the pion loop diagrams in Figs. 7 and 8 we use the proper-time regularization scheme; however, in this case the pions should not be confined and we therefore set $\Lambda_{\rm IR} = 0$ GeV. This procedure guarantees that the leading-order nonanalytic behavior of the hadron form factors as a function of the pion mass is retained.

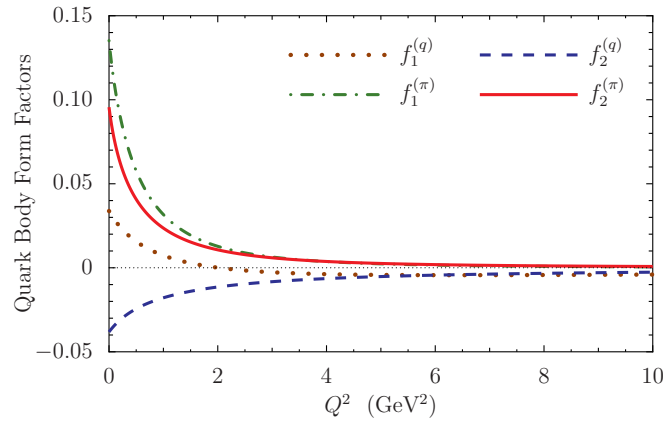

FIG. 9. (Color online) Dressed quark body form factors associated with the pion loop corrections, where $f_1^{(q)}$ and $f_2^{(q)}$ originate from the second diagram in Fig. 8 and $f_1^{(\pi)}$ and $f_2^{(\pi)}$ from the third diagram.

Results for the Dirac and Pauli dressed quark form factors, including pion loop effects, are given in Fig. 6. The pion cloud softens the Dirac form factors, however its most important consequence is the nonzero Pauli form factor for the dressed quarks. At infinite Q^2 the dressed quark Dirac form factors now become

$$F_{1U}(Q^2) \overset{Q^2\to\infty}{=} Z\, e_u, \quad F_{1D}(Q^2) \overset{Q^2\to\infty}{=} Z\, e_d, \tag{71}$$

whereas the Pauli form factors vanish for large Q^2. We find dressed quark anomalous magnetic moments of

$$\kappa_U = 0.10 \quad \text{and} \quad \kappa_D = -0.17, \tag{72}$$

defined as $\kappa_Q \equiv F_{2Q}(0)$. The quark charge and magnetic radii, defined with respect to the Sachs form factors and Eq. (48), take the values

$$r_E^U = 0.59 \text{ fm}, \quad r_M^U = 0.60 \text{ fm}, \tag{73}$$

$$r_E^D = 0.73 \text{ fm}, \quad r_M^D = 0.67 \text{ fm}. \tag{74}$$

Decomposing the dressed quark form factors in quark/flavor sectors gives

$$F_{1U}(Q^2) = e_u\, F_{1U}^u(Q^2) + e_d\, F_{1U}^d(Q^2), \tag{75}$$

$$F_{1D}(Q^2) = e_u\, F_{1D}^u(Q^2) + e_d\, F_{1D}^d(Q^2), \tag{76}$$

[12]The pion-quark-quark vertex in Fig. 7 can be read directly from the pion t matrix, given by Eq. (8), and takes the form $\gamma_5\,\tau_i$. A pseudovector component to the vertex would be generated through π–a_1 mixing in the BSE kernel; however, the strength of this vertex is suppressed by $m_\pi/m_{a_1} \sim 0.1$ relative to the dominant pseudoscalar component. Therefore, we do not include a π–a_1 mixing in the pion-quark-quark vertex.

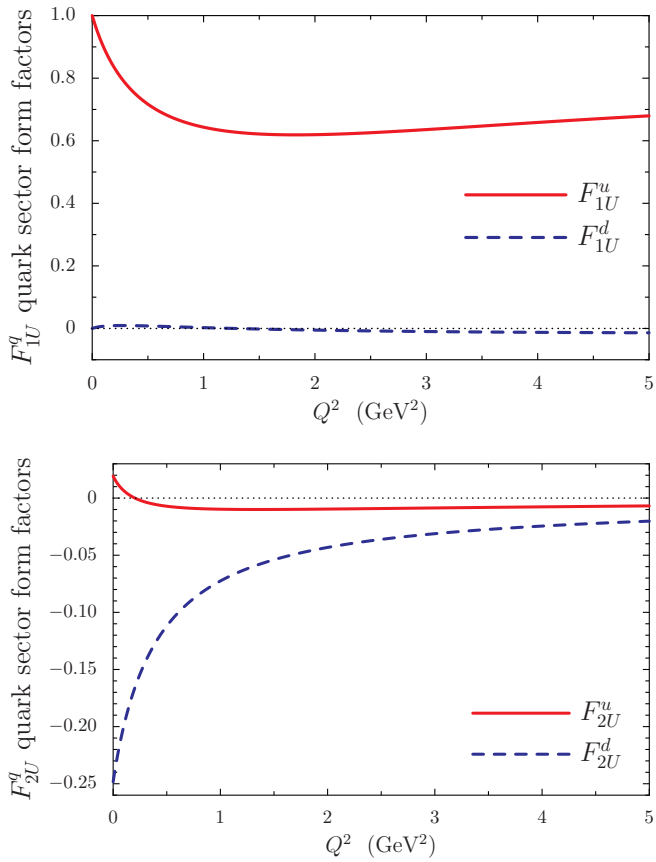

FIG. 10. (Color online) (Top) Dressed-up quark Dirac form factors, which also include pion-cloud effects, separated into quark sectors. The solid line is the u-quark sector of the dressed-up quark and the dashed line represents d-quark sector. (Bottom) Dressed-up quark Pauli form factors separated into quark sectors. The solid line is the u-quark sector and the dashed line the d-quark sector.

where the flavor sector dressed-up quark form factors read

$$F^u_{1U} = Z\,\tfrac{1}{2}[F_{1\omega} + F_{1\rho}] + [3\,F_{1\omega} - F_{1\rho}]f_1^{(q)} + F_{1\rho}\,f_1^{(\pi)}, \tag{77}$$

$$F^d_{1U} = Z\,\tfrac{1}{2}[F_{1\omega} - F_{1\rho}] + [3\,F_{1\omega} + F_{1\rho}]f_1^{(q)} - F_{1\rho}\,f_1^{(\pi)}, \tag{78}$$

$$F^u_{2U} = [3\,F_{1\omega} - F_{1\rho}]f_2^{(q)} + F_{1\rho}\,f_2^{(\pi)}, \tag{79}$$

$$F^d_{2U} = [3\,F_{1\omega} + F_{1\rho}]f_2^{(q)} - F_{1\rho}\,f_2^{(\pi)}. \tag{80}$$

The flavor sector dressed-down quark form factors are given by

$$F^u_{iD} = F^d_{iU} \quad \text{and} \quad F^d_{iD} = F^u_{iU}, \tag{81}$$

where $i = (1, 2)$. Therefore, these results satisfy charge symmetry and are illustrated in Fig. 10. For the quark-sector anomalous magnetic moments we find

$$\kappa^u_U = 0.02 \quad \text{and} \quad \kappa^d_U = -0.25, \tag{82}$$

and therefore the d current quarks carry the bulk of the dressed-up quark anomalous magnetic moment. This will have important implications for the nucleon form factors.

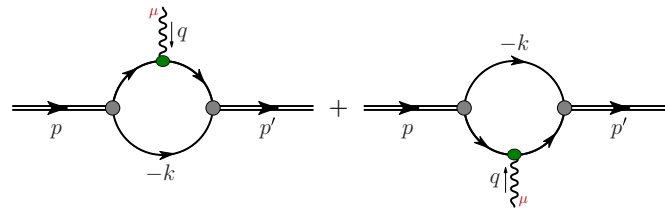

FIG. 11. (Color online) Feynman diagrams that represent the diquark electromagnetic current. The shaded circles are the diquark Bethe-Salpeter vertices and the shaded ovals are the quark-photon vertex. The Feynman diagrams for the meson form factors are analogous. However, the flow of baryon number on one of the quark lines must be reversed.

V. DIQUARK AND MESON FORM FACTORS

Critical to our picture of nucleon structure are diquark correlations inside the nucleon. An essential step, therefore, in calculating the nucleon form factors is to first determine the interaction of the virtual photon with the diquarks. A further reason to discuss the diquark form factors is that the scalar and axial-vector diquarks are the qq analogs of the π and ρ mesons.

The electromagnetic current of a diquark is represented by the Feynman diagrams illustrated in Fig. 11 and is expressed as

$$j^\mu(p',p) = i\int \frac{d^4k}{(2\pi)^4}\mathrm{Tr}[\overline{\Gamma}(p')\,S(p'+k)\,\Lambda^\mu_{\gamma Q}(p',p) \times S(p+k)\Gamma(p)\,S^T(-k)], \tag{83}$$

where the superscript T indicates transpose. The Bethe-Salpeter vertices are represented by $\Gamma(p)$ and are given in Eq. (27). The dressed quark-photon vertex $\Lambda^\mu_{\gamma Q}(p',p)$ is given in Eqs. (54) and (66).

Hadron form factors are determined using the three variants for the dressed quark form factors discussed in Sec. IV and illustrated, for the nontrivial variants, in Fig. 6. Results obtained by treating the dressed quarks as pointlike will be labeled with a superscript (bare), while those obtained using the dressed quark form factors from the BSE [Eq. (61)] will be labeled with a superscript (bse) and our full results, where the quark form factors also include pion loop corrections, Eqs. (67)–(70), will have no superscript label.

The electromagnetic current for a scalar diquark, or any on-shell spin-0 particle, has the general form

$$j^\mu_s(p',p) = (p'+p)^\mu\,F_s(Q^2) \tag{84}$$

and is therefore parametrized by a single form factor. Evaluating Eq. (83) for the scalar diquark gives

$$F_s(Q^2) = [F_{1U}(Q^2) + F_{1D}(Q^2)]f_s^V(Q^2) + [F_{2U}(Q^2) + F_{2D}(Q^2)]f_s^T(Q^2), \tag{85}$$

where f_s^V, f_s^T are the scalar diquark body form factors associated with the vector and tensor photon couplings to the dressed quarks [see Eq. (66)]. Results for the scalar diquark form factor are given in Fig. 12 for the three variants of dressed quark form factors. Vertex corrections introduced by the BSE

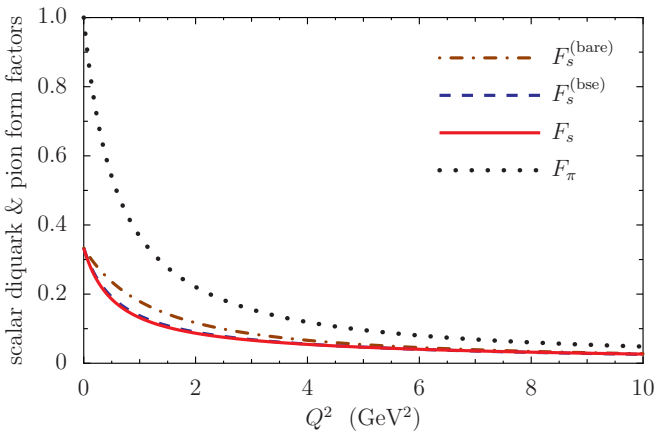

FIG. 12. (Color online) Results for the scalar diquark and pion form factors. For the pion we just show the full results; however, for the scalar diquark form factors we show the cases when the dressed quarks are pointlike, the quark-photon vertex is given by the BSE and finally when pion loop corrections are also included.

result in a softer form factor (dashed line) in comparison with results obtained using pointlike dressed quark form factors (dash-dotted line). Including pion loop corrections only slightly alters the scalar diquark form factor (solid line).

The $\bar{q}q$ analog of the scalar diquark is the pion, where for the π^+ the electromagnetic form factor is given by

$$F_\pi(Q^2) = [F_{1U}(Q^2) - F_{1D}(Q^2)]f_s^V(Q^2) + [F_{2U}(Q^2) - F_{2D}(Q^2)]f_s^T(Q^2). \quad (86)$$

The body form factors in Eq. (86) are the same as those for the scalar diquark, except they are now functions of the pion mass instead of the scalar diquark mass.[13] We do not include pion loop corrections on the dressed quarks in the case of the pion form factor, because at the hadronic level there is no three pion vertex. The full result for the pion form factor is given as the dotted curve in Fig. 12. The scalar diquark and pion form factors multiplied by Q^2 are presented in Fig. 13, where good agreement with pion form-factor data from Refs. [59–63] is seen. At large Q^2 both form factors plateau, where we find $Q^2 F_\pi(Q^2) \to 0.48$ and $Q^2 F_s(Q^2) \to 0.30$. The pion form-factor result is consistent with the perturbative QCD prediction [64,65],

$$Q^2 F_\pi(Q^2) \overset{Q^2\to\infty}{\longrightarrow} 16\pi f_\pi^2 \alpha_s(Q^2), \quad (87)$$

in the sense that the strong coupling constant, $\alpha_s(Q^2)$, corresponds to a constant in the NJL model and therefore $Q^2 F_\pi(Q^2)$ should become constant as $Q^2 \to \infty$. Taking Eq. (87) literally, our pion form-factor result implies that $\alpha_s(Q^2) = 1.12$, which using a NNLO result for the running coupling [66] would correspond to an NJL model scale of $Q_0^2 \sim 0.18$ GeV^2, which is consistent with previous estimates

[13]There is also a factor of two because of the different definition for the Bethe-Salpeter normalization given in Eq. (18), compared to that in Eq. (28).

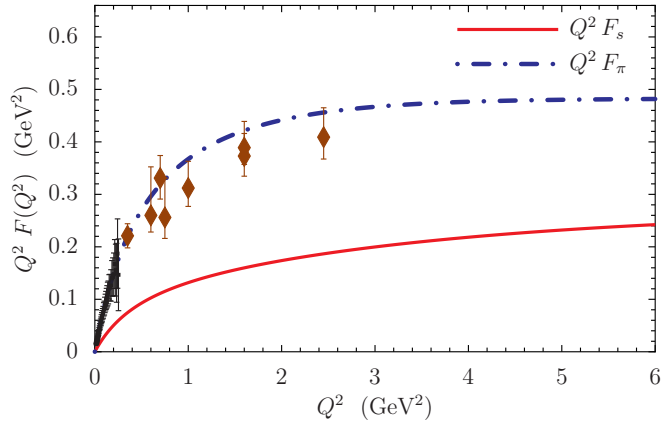

FIG. 13. (Color online) Scalar diquark and pion form factors multiplied by Q^2. The pion form-factor data is from Refs. [59–63].

[30–32]. Our calculated pion form factor reaches its plateau by $Q^2 \simeq 6$ GeV^2, which corresponds to the same scale at which the Dyson-Schwinger equation results of Ref. [67] reach a maximum, after which the result of Ref. [67] decreases because of the logarithmic running of $\alpha_s(Q^2)$ in QCD.

Results for the scalar diquark and pion charge radii are given in Table II for the three variants of the dressed quark form factors. The charge radius of the pion and scalar diquark are found to be very similar, where the pion radius is approximately 5% smaller than the experimental value from Refs. [59,68].

The electromagnetic current for an axial-vector diquark, or any on-shell spin-1 particle, has the general form [69]

$$j_a^{\mu,\alpha\beta}(p',p) = \left[g^{\alpha\beta}F_{1a}(Q^2) - \frac{q^\alpha q^\beta}{2M_a^2}F_{2a}(Q^2)\right](p'+p)^\mu - (q^\alpha g^{\mu\beta} - q^\beta g^{\mu\alpha})F_{3a}(Q^2), \quad (88)$$

where the Lorentz indices μ, α, β represent the polarizations of the photon, initial axial-vector diquark, and final axial-vector diquark, respectively. The Lorentz covariant form factors of Eq. (88) are often reexpressed as the Sachs-like charge, magnetic, and quadruple form factors for a spin-1 particle, given by

$$G_C(Q^2) = F_1(Q^2) + \tfrac{2}{3}\eta G_Q(Q^2), \quad (89)$$

$$G_M(Q^2) = F_3(Q^2), \quad (90)$$

$$G_Q(Q^2) = F_1(Q^2) + (1+\eta)F_2(Q^2) - F_3(Q^2), \quad (91)$$

TABLE II. Charge radii for the scalar diquark and pion, each shown for the three variants for the dressed quark form factors. The experimental value for the pion is from Refs. [59,68]. All radii are in units of fm.

	$r_E^{(\mathrm{bare})}$	$r_E^{(\mathrm{bse})}$	r_E	r_E^{exp}
Scalar diquark	0.46	0.62	0.63	
Pion	0.46	0.62	0.62	0.663 ± 0.006

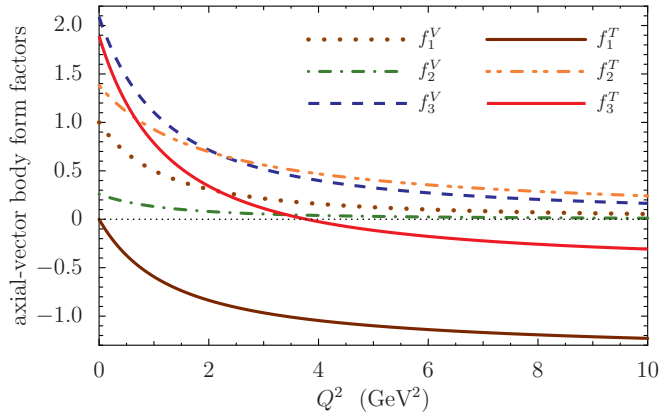

FIG. 14. (Color online) Axial-vector diquark body form factors. These body form factors must still be multiplied by the appropriate dressed quark form factors to obtain the axial-vector diquark form factors.

where $\eta = \frac{Q^2}{4m_H^2}$ and m_H is the relevant hadron mass. At $Q^2 = 0$ these form factors give, respectively, the charge, magnetic moment, and quadruple moment of a spin-one particle, in units of e, $e/(2m_H)$, and e/m_H^2. The charge, magnetic, and quadrupole radii—$\langle r_C^2\rangle$, $\langle r_M^2\rangle$, $\langle r_Q^2\rangle$—are defined with respect to these Sachs-like form factors.

Evaluating the Feynman diagrams of Fig. 11, using the axial-vector diquark Bethe-Salpeter vertex given in Eq. (27) and the quark-photon vertex of Eq. (54) gives, for an axial-vector diquark with quark content $\{ud\}$, the form-factor result

$$F_{ia}^{\{ud\}}(Q^2) = [F_{1U}(Q^2) + F_{1D}(Q^2)]f_i^V(Q^2) + [F_{2U}(Q^2) + F_{2D}(Q^2)]f_i^T(Q^2), \quad (92)$$

where $i \in 1, 2, 3$ correspond to the form factors in Eq. (88). Expressions for axial-vector diquarks of the $\{uu\}$ and $\{dd\}$ type are simply given by Eq. (92) with the appropriate substitution of the dressed quark form factors. The vector and tensor body form factors, f_i^V and f_i^T, are illustrated in Fig. 14. A notable feature of these form factors is that charge conservation implies $f_1^V(0) = 1$ and $f_1^T(0) = 0$. The magnetic moment equals $f_3^V(0) = 2.09$, which, because of relativistic effects, is slightly larger than the canonical value of $\mu_1 = 2$ for a spin-1 particle. For the quadrupole moment the body form factors imply $\mathcal{Q} = -0.83$, which, because of relativistic effects, is about 17% smaller than the canonical value of $\mathcal{Q} = -1$.

Results for the form factors of Eq. (88) for an axial-vector diquark with quark content $\{ud\}$ are presented in Fig. 15. In each case the vertex dressing from the quark-photon inhomogeneous BSE results in a softening of form factors, compared to the case of pointlike dressed quarks. Although the pion loop effects leave F_{1a} almost unchanged, both F_{2a} and F_{3a} receive sizable negative corrections. The origin of these corrections can be traced back to Eq. (88) and the results in Fig. 14. The tensor body from factors f_2^T and f_3^T are large and positive for small Q^2. This, together with the large negative anomalous magnetic moment of the dressed-down quark [see Eq. (72)], results in sizable corrections to F_{2a} and F_{3a} from pion loop effects.

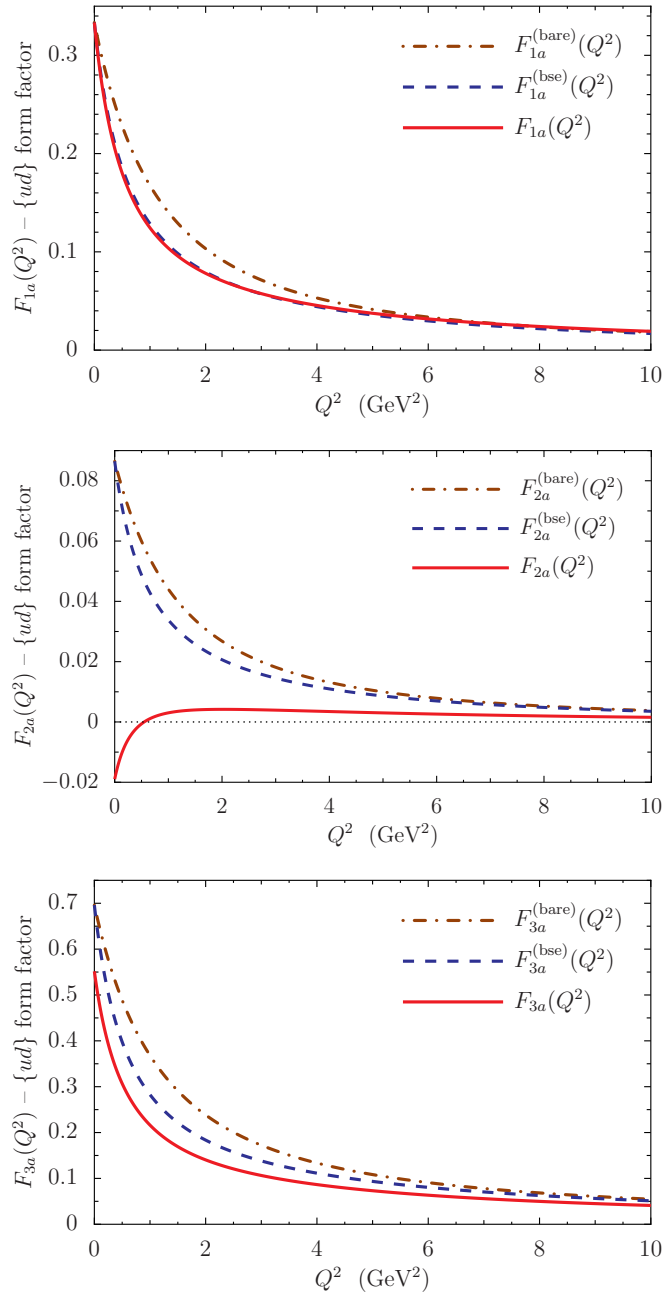

FIG. 15. (Color online) Form factors for an axial-vector diquark with quark content $\{ud\}$.

The Lorentz covariant form factors for the ρ^+ meson, associated with the current of Eq. (88), are given by

$$F_{i\rho}(Q^2) = [F_{1U}(Q^2) - F_{1D}(Q^2)]f_i^V(Q^2) + [F_{2U}(Q^2) - F_{2D}(Q^2)]f_i^T(Q^2), \quad (93)$$

where $i \in 1, 2, 3$ and the body form factors are now functions of the ρ mass instead of the axial-vector diquark mass. Results for the Sachs-like spin-1 form factors defined in Eqs. (89)–(91) are illustrated in Fig. 16 for a $\{ud\}$-type axial-vector diquark and the ρ^+ meson. In these figures we only show the full results which include pion-cloud effects. The zero in the charge form

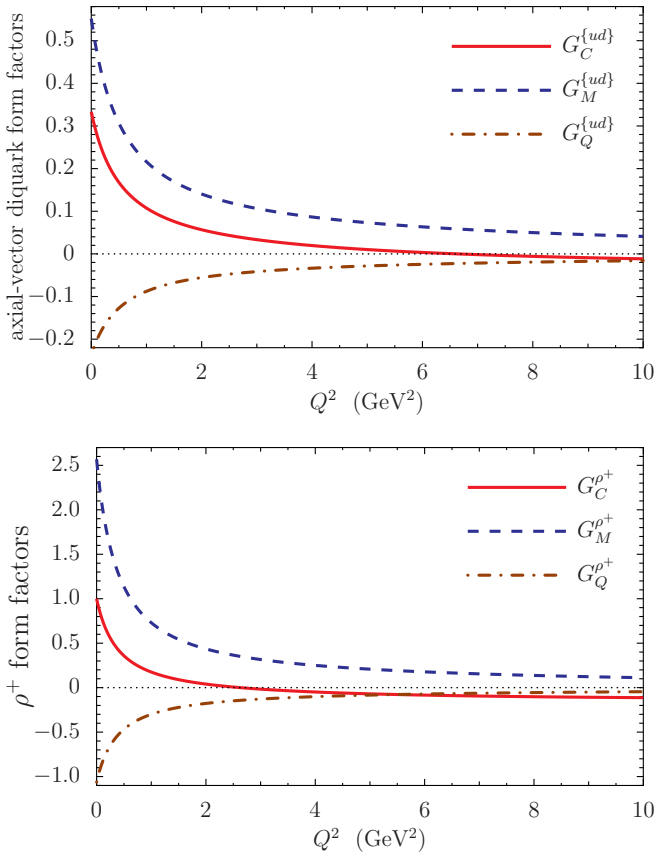

FIG. 16. (Color online) (Top) results for the charge, magnetic, and quadruple form factors of a ud axial-vector diquark. (Bottom) results for the charge, magnetic and quadruple form factors of a ρ^+ meson.

factors occurs at $Q^2 \simeq 6.6\ \mathrm{GeV}^2$ for $G_C^{\{ud\}}$ and for $G_C^{\rho^+}$ at $Q^2 \simeq 2.6\ \mathrm{GeV}^2$.

Static properties of the ρ^+ and the axial-vector diquarks are given Table III for variants of the dressed quark form factors. We find that pion loop effects have a substantial impact on the static properties of the axial-vector diquarks and ρ mesons. For example, the pion cloud increases the magnitude of the ρ^+ magnetic moment by 24% and the quadrupole moment by 22%, while for the $\{ud\}$-type axial-vector diquarks we find a reduction of the magnetic moment by 21% and the magnitude of the quadrupole moment by 14%. The sign difference between these corrections for the ρ^+ and $\{ud\}$-type axial-vector diquark arises because the dressed-down quark form factors enter the respective currents with the opposite sign—see Eqs. (92) and (93)—and the dressed-down quark has a large anomalous magnetic moment. For the ρ^+ meson the pion cloud uniformly increases the charge, magnetic, and quadrupole radii by approximately 16%, whereas for the $\{ud\}$-type axial-vector diquarks the pion cloud has little effect on the charge and quadrupole radii but increases the magnetic radius by 38%.

As an interesting check on the large Q^2 behavior of our ρ or axial-vector diquark form-factor results, we make a comparison with the relations derived in Ref. [70]. That is, at large timelike or spacelike momenta, the ratio of the form factors for a spin-1 particle should behave as

$$G_C(Q^2) : G_M(Q^2) : G_Q(Q^2) = \left(1 - \tfrac{2}{3}\eta\right) : 2 : -1, \quad (94)$$

where corrections are of the orders Λ_{QCD}/Q and $\Lambda_{\mathrm{QCD}}/M_\rho$. For our spin-1 results we find that the G_C/G_Q constraint is satisfied to better than 15% for $Q^2 = 10\ \mathrm{GeV}^2$ and to better than 3% for $Q^2 = 100\ \mathrm{GeV}^2$; for $Q^2 > 1000\ \mathrm{GeV}^2$ our result takes the value given in Eq. (94). The calculated ratios G_C/G_M and G_M/G_Q saturate within 15% of the values in Eq. (94). However, this deviation is well within the leading correction of $\Lambda_{\mathrm{QCD}}/M_\rho \sim 0.3$.

The remaining diquark electromagnetic current that contributes to the nucleon form factors is the transition current between scalar and axial-vector diquarks. This current has the form

$$j_{sa}^{\mu,\alpha}(p',p) = \pm \frac{1}{M_s + M_a}\, i\varepsilon^{\alpha\mu\sigma\lambda} p'_\sigma p_\lambda\, F_{sa}(Q^2), \quad (95)$$

where the plus sign indicates a scalar $\to$ axial$-$vector transition and the reverse process has the minus sign. The Lorentz indices μ and α represent the polarizations of the photon and the axial-vector diquark. Evaluating the Feynman diagram of Fig. 11 for this transition process gives

$$F_{sa}(Q^2) = [F_{1U}(Q^2) - F_{1D}(Q^2)] f_{sa}^V(Q^2) + [F_{2U}(Q^2) - F_{2D}(Q^2)] f_{sa}^T(Q^2), \quad (96)$$

where $f_{sa}^V(Q^2)$ and $f_{sa}^T(Q^2)$ are the vector and tensor body form factors. The electromagnetic transition form factor describing the $\gamma^*\pi^+ \to \rho^+$ process is given by

$$F_{\pi\rho}(Q^2) = [F_{1U}(Q^2) + F_{1D}(Q^2)] f_{sa}^V(Q^2) + [F_{2U}(Q^2) + F_{2D}(Q^2)] f_{sa}^T(Q^2), \quad (97)$$

TABLE III. Results for the magnetic moment, quadruple moment, and the charge, magnetic, and quadruple radius of the axial-vector diquarks and ρ^+ meson. In each case we present results for various levels of sophistication for the constituent quark form factors. All radii are in units of fm; the magnetic moment has units $e/(2m_H)$ and the quadruple moment e/m_H^2, where m_H is the mass of the relevant diquark or meson.

	$\mu^{(\mathrm{bse})}$	μ	$\mathcal{Q}^{(\mathrm{bse})}$	$\mathcal{Q}$	$r_C^{(\mathrm{bse})}$	r_C	$r_M^{(\mathrm{bse})}$	r_M	$r_Q^{(\mathrm{bse})}$	r_Q
$\{uu\}$ axial-vector diquark	2.78	3.14	−1.10	−1.20	0.65	0.76	0.61	0.74	0.61	0.74
$\{ud\}$ axial-vector diquark	0.70	0.55	−0.28	−0.24	0.37	0.38	0.60	0.62	0.61	0.64
$\{dd\}$ axial-vector diquark	−1.39	−2.04	0.55	0.73	0.65	0.84	0.61	0.80	0.62	0.79
ρ^+	2.08	2.57	−0.87	−1.06	0.67	0.82	0.62	0.77	0.62	0.77

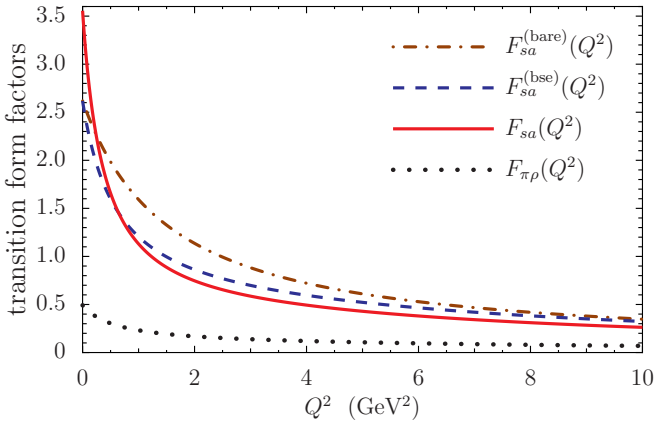

FIG. 17. (Color online) Results for the scalar $\leftrightarrow$ axial−vector diquark and $\pi \leftrightarrow \rho$ electromagnetic transition form factors.

where body form factors are now functions of the π and ρ masses. Results for F_{sa} and $F_{\pi\rho}$ are presented in Fig. 17. The vertex dressing from the BSE produces a softer form factor, and for the diquark transition the large isovector combination of the constituent quark Pauli form factors, arising from the pion cloud, gives a sizable correction for $Q^2 \lesssim 1\,\mathrm{GeV}^2$. Results for the transition moment and transition radius are given in Table IV.

VI. NUCLEON FORM-FACTOR RESULTS

The Feynman diagrams that contribute to the nucleon's electromagnetic current are illustrated in Fig. 4, where the coupling of the photon to the dressed quarks and diquarks has been discussed in Secs. IV and V, respectively. Using a quark-photon vertex of the form given in Eq. (54) demarcates the nucleon form factors into flavor sectors defined by the dressed quarks, such that

$$F_{ip}(Q^2) = F_{ip}^U(Q^2) + F_{ip}^D(Q^2), \tag{98}$$

$$F_{in}(Q^2) = F_{in}^U(Q^2) + F_{in}^D(Q^2), \tag{99}$$

where $i = (1, 2)$. The dressed quark flavor-sector nucleon form factors are given by the product of dressed quark form factors [e.g., Eqs. (67)–(70)] with the nucleon body form factors, such that

$$F_{ip}^{\mathcal{Q}} = F_{1\mathcal{Q}}\, f_{ip}^{\mathcal{Q},V} + F_{2\mathcal{Q}}\, f_{ip}^{\mathcal{Q},T}, \tag{100}$$

$$F_{in}^{\mathcal{Q}} = F_{1\mathcal{Q}}\, f_{in}^{\mathcal{Q},V} + F_{2\mathcal{Q}}\, f_{in}^{\mathcal{Q},T}, \tag{101}$$

TABLE IV. Results for the transition moment, defined as $\kappa_T \equiv F(0)$, the transition radius (which is normalized by κ_T), for scalar $\leftrightarrow$ axial−vector diquark and pion $\leftrightarrow$ ρ transitions. Radii are in units of fm.

	$\kappa_T^{(\mathrm{bse})}$	κ_T	$r_T^{(\mathrm{bse})}$	r_T
$s \leftrightarrow a$	2.66	3.61	0.75	0.99
$\pi \leftrightarrow \rho$	0.62	0.49	0.54	0.54

where $\mathcal{Q} = (U, D)$ and the Q^2 dependence of each form factor has been omitted. The superscript V indicates a vector body form factor and the superscript T a tensor body form factor, which arise from the quark current of Eq. (66).

The proton body form factors in Eq. (100), which represent the sum of the six Feynman diagrams of Fig. 4, have the structure

$$f_{ip}^{U,V} = f_{i\mathcal{Q}}^{s,V} + \tfrac{1}{3} f_{i\mathcal{Q}}^{a,V} + f_{i\mathcal{D}}^{s,V} + \tfrac{5}{3} f_{i\mathcal{D}}^{a,V} + \tfrac{1}{\sqrt{3}} f_{i\mathcal{D}}^{sa,V}, \tag{102}$$

$$f_{ip}^{D,V} = \tfrac{2}{3} f_{i\mathcal{Q}}^{a,V} + f_{i\mathcal{D}}^{s,V} + \tfrac{1}{3} f_{i\mathcal{D}}^{a,V} - \tfrac{1}{\sqrt{3}} f_{i\mathcal{D}}^{sa,V}. \tag{103}$$

For equal current quark masses the neutron body form factors in Eq. (101) are given by

$$f_{in}^{D,V} = f_{ip}^{U,V} \quad \text{and} \quad f_{in}^{U,V} = f_{ip}^{D,V}, \tag{104}$$

and therefore the nucleon body form factors satisfy the constraints imposed by charge symmetry. Expressions for the nucleon tensor body form factors are obtained from Eqs. (102)–(104) with $V \to T$. The nomenclature for these nucleon body form factors is as follows: A subscript $\mathcal{Q}$ implies that the photon couples directly to a quark (*quark diagram*) and a subscript $\mathcal{D}$ implies that the photon couples to (a quark inside) a diquark (*diquark diagram*); a superscript s indicates that the diagram contains only a scalar diquark, while the superscript a only an axial-vector diquark and the superscript sa implies the sum of the two diagrams where a photon induces a transition between scalar and axial-vector diquarks. The numerical coefficients in Eqs. (102) and (103) arise from the isospin structure of the proton Faddeev and the quark-photon vertices, given in Eqs. (30) and (54), respectively.

Nucleon body form-factor results for each diagram in Fig. 4, as expressed by Eqs. (102) and (103), are presented in Fig. 18 for the vector coupling to the dressed quarks and in Fig. 19 for the tensor coupling. Table V gives the $Q^2 = 0$ values of the nucleon body form factors. Charge conservation for the vector coupling implies that in this case diagrams with the same quark-diquark content must be equal at $Q^2 = 0$. Furthermore, with the normalization used here, the sum of quark diagrams and of diquark diagrams must each equal one in the vector case. For the vector coupling, charge conservation also forbids the scalar–axial-vector diquark diagram (sa) from contributing to the charge. However, this diagram does give an important contribution to the nucleon anomalous magnetic moment. For the vector coupling diagrams the only object with a magnetic moment is the axial-vector diquark. Thus, the nonzero values for the other f_2 body form-factor diagrams, in the bottom panel of Fig. 18, indicate that the associated pieces of the nucleon wave function have sizable p and d wave components. Therefore, the nucleon wave function contains a significant amount of quark orbital angular momentum.

Figure 19 and Table V demonstrate that the tensor coupling diagrams do not contribute to the nucleon charge, which is consistent with constraints imposed by the Ward-Takahashi identity for the nucleon electromagnetic current. However, these diagrams do have an important impact on the anomalous magnetic moment. The Q^2 behavior of the form factors is also influenced by the tensor coupling diagrams. However,

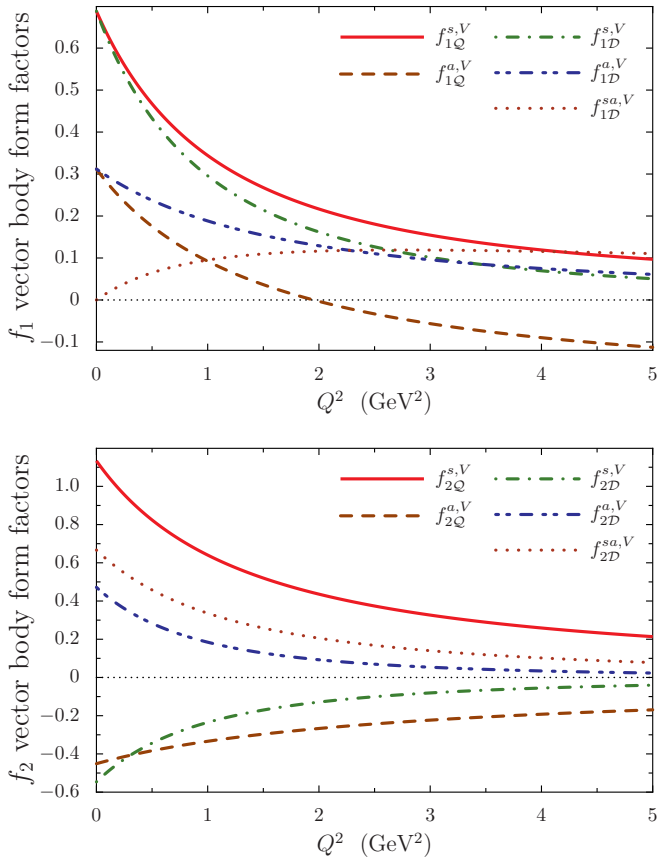

FIG. 18. (Color online) Nucleon Dirac (top) and Pauli (bottom) body form factors which result from a vector coupling to the quarks in the Feynman diagrams of Fig. 4. To obtain their contribution to the nucleon form factors these results must be multiplied by the appropriate isospin factors, as in Eqs. (102) and (103), and the dressed quark Dirac form factors.

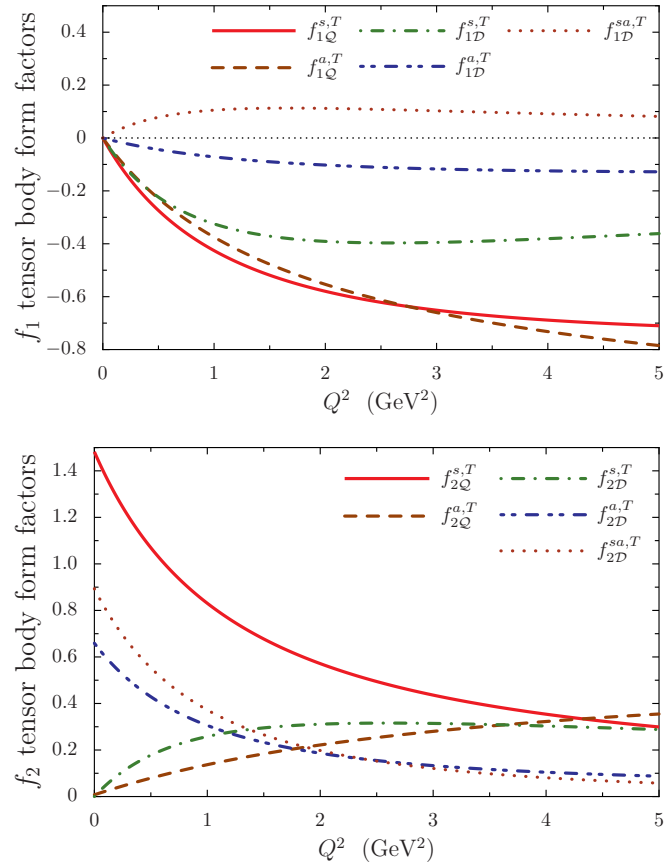

FIG. 19. (Color online) Nucleon Dirac (top) and Pauli (bottom) body form factors which result from a tensor coupling to the quarks in the Feynman diagrams of Fig. 4. To obtain their contribution to the nucleon form factors these results must be multiplied by the appropriate isospin factors, as in Eqs. (102) and (103), and the dressed quark Pauli form factors.

once multiplied by the dressed quark Pauli form factors, their contribution diminishes rapidly with Q^2, being of little importance for $Q^2 \gtrsim 1$ GeV^2.

In Sec. II the nucleon Faddeev equation was solved by first making a pole approximation for the diquark t matrices; see, for example, Eqs. (38) and (39). For a consistent nucleon form-factor calculation we must therefore approximate all two-body t matrices by their pole form, which also includes the quark-photon vertex obtained from the inhomogeneous BSE illustrated in Fig. 5. Expressing $\Pi_{VV}(q^2) = q^2\,\hat{\Pi}_{VV}(q^2)$ in Eq. (60) and expanding $\hat{\Pi}_{VV}(q^2)$ about either the ρ or ω pole mass, we obtain results for the pole forms of the BSE form factors,

$$F_{1i}(Q^2) = \frac{1}{1 + Q^2/m_i^2}, \qquad i \in \omega, \rho, \tag{105}$$

which is the familiar vector meson dominance result. The dressed quark form factors therefore maintain the vector meson pole structure in the timelike region obtained in the original BSE results of Eq. (60). For the nucleon form-factor

TABLE V. Nucleon Dirac and Pauli body form factors evaluated at $Q^2 = 0$. The subscript $i = 1,2$ corresponds to either the first or the second row of the table. An entry with only one significant figure takes that exact value because of charge conservation. The last four columns give results for the vector and tensor versions of Eqs. (102) and (103) at $Q^2 = 0$. To obtain nucleon form-factor results at $Q^2 = 0$ these results must be multiplied the by appropriate quark charge for the vector coupling diagrams and by the appropriate dressed quark anomalous magnetic moment for the tensor coupling diagrams.

	$f^{s,V}_{i\mathcal{Q}}$	$f^{a,V}_{i\mathcal{Q}}$	$f^{s,V}_{i\mathcal{D}}$	$f^{a,V}_{i\mathcal{D}}$	$f^{sa,V}_{i\mathcal{D}}$	$f^{s,T}_{i\mathcal{Q}}$	$f^{a,T}_{i\mathcal{Q}}$	$f^{s,T}_{i\mathcal{D}}$	$f^{a,T}_{i\mathcal{D}}$	$f^{sa,T}_{i\mathcal{D}}$	$f^{U,V}_{ip}$	$f^{D,V}_{ip}$	$f^{U,T}_{ip}$	$f^{D,T}_{ip}$
Dirac	0.688	0.312	0.688	0.312	0	0	0	0	0	0	2	1	0	0
Pauli	1.134	−0.451	−0.546	0.472	0.666	1.482	0.008	0.0	0.659	0.893	1.61	−1.07	3.10	−0.29

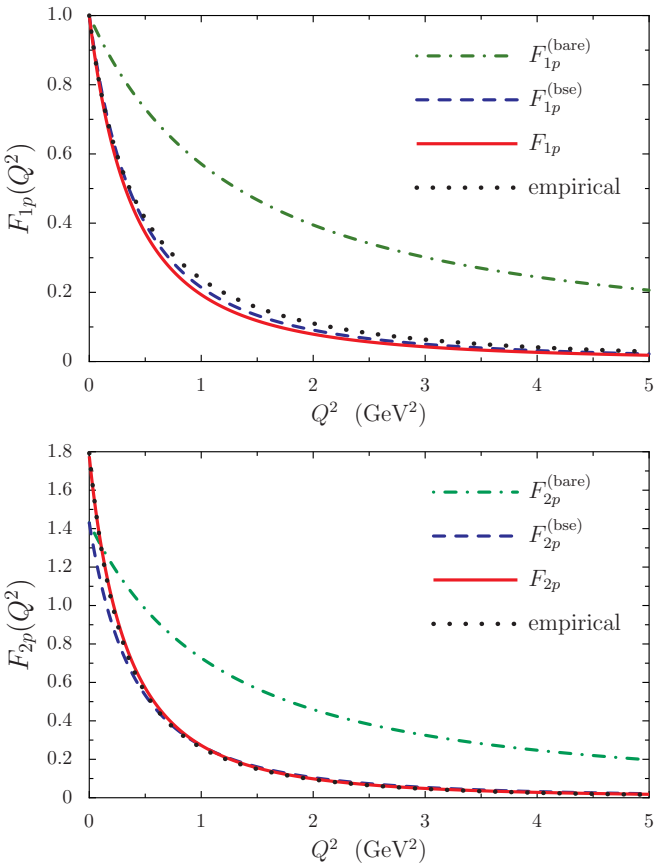

FIG. 20. (Color online) Results for the proton Dirac (top) and Pauli (bottom) form factors. In each case the dot-dashed curve [superscript (bare)] gives the result when the constituent quark form factors are those of an elementary Dirac particle, the dashed curve [superscript (bse)] includes the quark-photon vertex dressing effects from the BSE, and the solid curve is the full result which also includes pion loop effects. The dotted curve is the empirical result from Ref. [71].

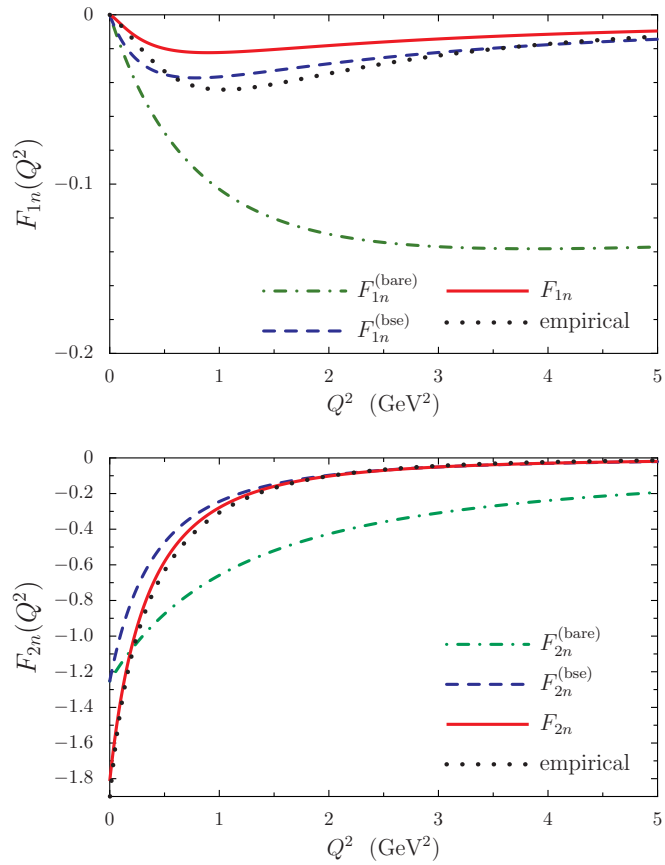

FIG. 21. (Color online) Results for the neutron Dirac (top) and Pauli (bottom) form factors. In each case the dot-dashed curve [superscript (bare)] gives the results when the constituent quark form factors are those of an elementary Dirac particle, the dashed curve [superscript (bse)] includes the quark-photon vertex dressing effects from the BSE, and the solid curve is the full result which also includes pion loop effects. The dotted curve is the empirical result from Ref. [71].

calculations the result in Eq. (105) will replace the full BSE result of Eq. (60) used in the dressed quark form factors, for example, in Eq. (61) and Eqs. (67)–(70).

Dirac and Pauli form-factor results for the proton and neutron are presented in Figs. 20 and 21, respectively, while results for the Sachs form factors are given in Figs. 22 and 23. The three curves in each figure represent results for the three variants of the dressed quark form factors used in Eqs. (98)–(101). The dot-dashed curves are the results where the dressed quarks are treated as pointlike and therefore their Dirac form factors are constants equal to the quark charges and the Pauli form factors are zero. These results are labeled with the superscript (bare). Results for the nucleon form factors that include the dressing of the quark-photon vertex by vector mesons, generated by Eq. (105), are illustrated by the dashed lines with the superscript (bse). Finally, we use dressed quark form factors that also incorporate effects from pion loops, which generate a nonzero Pauli form factor for the dressed quarks. These results are illustrated as the solid lines (without a superscript label).

The full results for the nucleon form factors, including pion loop effects, display good agreement with the empirical parametrizations from Ref. [71], which are illustrated as the dotted curves in Figs. 20 through 23. Both the proton and the neutron Dirac form factor are slightly softer than the empirical parametrizations, whereas the Pauli form factors are in almost perfect agreement. The dressing of the quark-photon vertex by the pole form of the BSE [Eq. (105)] results in a significant softening of all nucleon form factors, proving critical for a realistic Q^2 dependence of the form factors. Pion loop corrections result in a further 50% reduction of the neutron Dirac form factor for low to moderate Q^2 and significantly enhance the nucleon Pauli form factors for $Q^2 \lesssim 1$ GeV^2. These enhancements correspond to increases in the magnitude of the proton and neutron anomalous magnetic moments by 25% and 45%, as indicated in Table VI. For the proton and neutron magnetic moments we find $\mu_p = 2.78\ \mu_N$ and $\mu_n = -1.81\ \mu_N$, which agree well with the experimental values of $\mu_p = 2.793\ \mu_N$ and $\mu_n = -1.913\ \mu_N$ [72]. To obtain the physical result $|\kappa_n| > \kappa_p$ for the nucleon anomalous

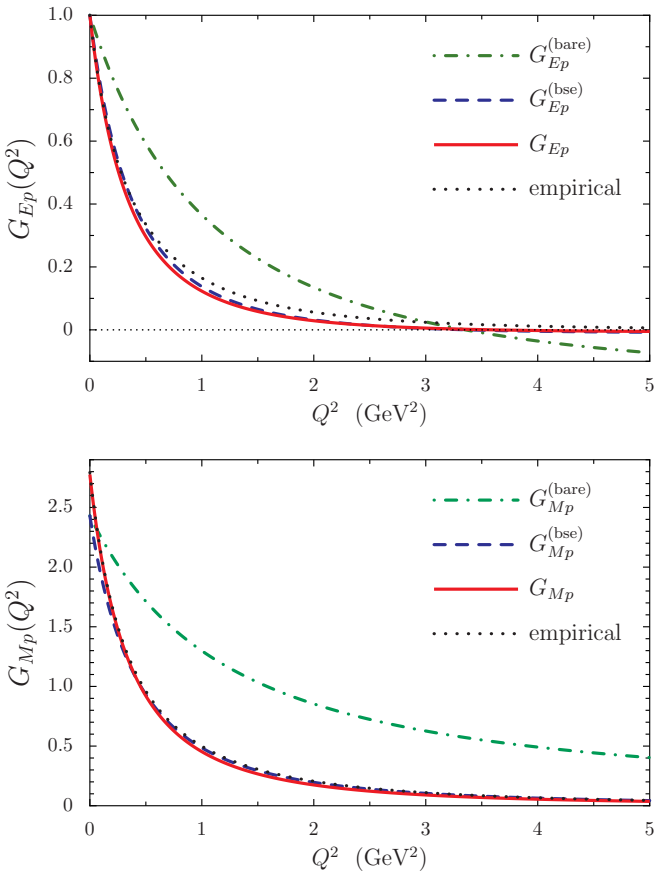

FIG. 22. (Color online) Results for the proton Sachs electric (top) and magnetic (bottom) form factors. In each case the dot-dashed curve [superscript (bare)] is the result when the constituent quark form factors are those of an elementary Dirac particle, the dashed curve [superscript (bse)] includes the quark-photon vertex dressing effects from the BSE, and the solid curve is the full result, which also includes pion loop effects. The dotted curve is the empirical result from Ref. [71].

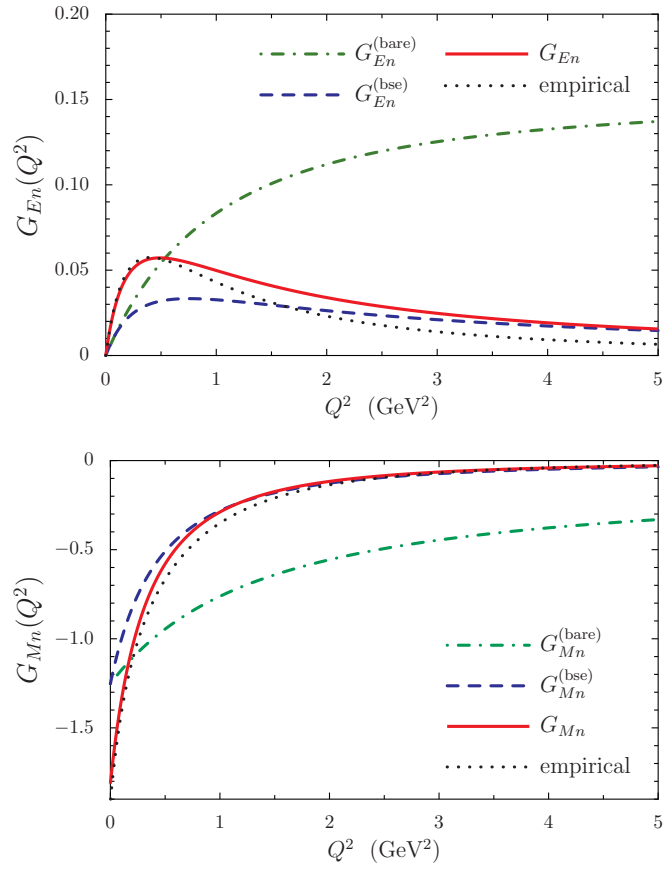

FIG. 23. (Color online) Results for the neutron Sachs electric (top) and magnetic (bottom) form factors. In each case the dot-dashed curve [superscript (bare)] is the results when the constituent quark form factors are those of an elementary Dirac particle, the dashed curve [superscript (bse)] includes the quark-photon vertex dressing effects from the BSE, and the solid curve is the full result which also includes pion loop effects. The dotted curve is the empirical result from Ref. [71].

magnetic moments, we find that the dressed quark anomalous magnetic moments of Eq. (72) are critical. In particular, κ_U must be positive and κ_D negative, with $|\kappa_D| > \kappa_U$. We obtain $|\kappa_D| > \kappa_U$ because the second diagram in Fig. 8 only contributes to the dressed-down quark anomalous magnetic moment [cf. Eqs. (69) and (70)], giving an additional negative contribution.

Results for the charge and magnetic radii, defined by Eqs. (49) and (50), are given in Table VI for the two cases where the dressed quark form factors are given by Eq. (105) and where pion loop effects are also included. The pion loop effects result in a 65% increase in magnitude of the neutron charge radius, a 19% increase in its magnetic radius, while the proton charge radius increases by 6% and the magnetic radius by 12%. All nucleon radii agree well with the empirical values taken from Ref. [71]. A recent global fit to data [73] found the proton charge and magnetic radius to be

$$r_{Ep} = 0.875 \pm 0.008(\mathrm{exp}) \pm 0.006(\mathrm{fit})\ \mathrm{fm}, \quad (106)$$

$$r_{Mp} = 0.867 \pm 0.009(\mathrm{exp}) \pm 0.018(\mathrm{fit})\ \mathrm{fm}, \quad (107)$$

and a recent Mainz experiment found [74]

$$r_{Ep} = 0.879\ (5)_{\mathrm{stat}}(4)_{\mathrm{syst}}(2)_{\mathrm{model}}(4)_{\mathrm{group}}\ \mathrm{fm}, \quad (108)$$

$$r_{Mp} = 0.777(13)_{\mathrm{stat}}(9)_{\mathrm{syst}}(5)_{\mathrm{model}}(2)_{\mathrm{group}}\ \mathrm{fm}. \quad (109)$$

Our proton results agree well with those of Ref. [73]. The origin of the sizable discrepancy between the two experimental results for the proton magnetic radius is discussed, for example, in Ref. [75]. In addition, in view of the muonic hydrogen controversy [10], the experimental errors quoted in both places appear to be rather low.

The flavor-sector nucleon form factors defined by the dressed quarks, as given in Eqs. (100) and (101), do not satisfy the standard charge symmetry relations, that is,

$$\frac{F_{ip}^U}{e_u} \neq \frac{F_{in}^D}{e_d} \quad \text{and} \quad \frac{F_{ip}^D}{e_d} \neq \frac{F_{in}^U}{e_u}, \quad (110)$$

TABLE VI. Results for the nucleon magnetic moments and radii, with dressed quark form factors given by Eqs. (61) and (105), labeled with a superscript (bse), and results that also include pion-cloud effects at the dressed quark level (these results do not carry a superscript label). Experimental results, labeled with a superscript exp, are taken from Ref. [71].

	$\mu^{(\mathrm{bse})}$	μ	μ^{exp}	$r_E^{(\mathrm{bse})}$	r_E	r_E^{exp}	$r_M^{(\mathrm{bse})}$	r_M	r_M^{exp}
Proton	2.43	2.78	2.793	0.81	0.86	0.863 ± 0.004	0.76	0.84	0.848 ± 0.003
Neutron	−1.25	−1.81	−1.913	−0.20	−0.34	-0.335 ± 0.055	0.74	0.88	0.907 ± 0.016

where $i = (1, 2)$.[14] The reason for this lies not with the nucleon body form factors, cf. Eq. (104), but with the form factors of the dressed quarks. Dressed quarks are quasiparticles that contain an infinite number of u and d current quarks. Hence, a dressed-up quark form factor, for example, contains contributions from both u and d current quarks. To obtain the nucleon quark-sector form factors, defined, in general, in Eq. (43), the dressed quark form factors must be expressed in their quark-sector form as given in Eqs. (77)–(80). The nucleon quark-sector form factors are therefore given by

$$F_{ip}^{q} = F_{1Q}^{q}\, f_{ip}^{Q,V} + F_{2Q}^{q}\, f_{ip}^{Q,T}, \tag{111}$$

$$F_{in}^{q} = F_{1Q}^{q}\, f_{in}^{Q,V} + F_{2Q}^{q}\, f_{in}^{Q,T}, \tag{112}$$

where $i = (1, 2)$, $q = (u, d)$, and there is an implied sum over $Q = (U, D)$. These results satisfy the charge symmetry constraints

$$F_{in}^{u} = F_{ip}^{d} \quad \text{and} \quad F_{in}^{d} = F_{ip}^{u}. \tag{113}$$

Quark-sector proton form-factor results are presented in Figs. 24 and 25 for the three stages of sophistication in the description of the dressed quark form factors. Empirical results, shown by the dotted lines, were obtained from Ref. [71] using Eq. (47). While the agreement between our

[14] Here we must divide out the quark charges because they are included in the definition of the dressed quark form factor; see Eqs. (100) and (101).

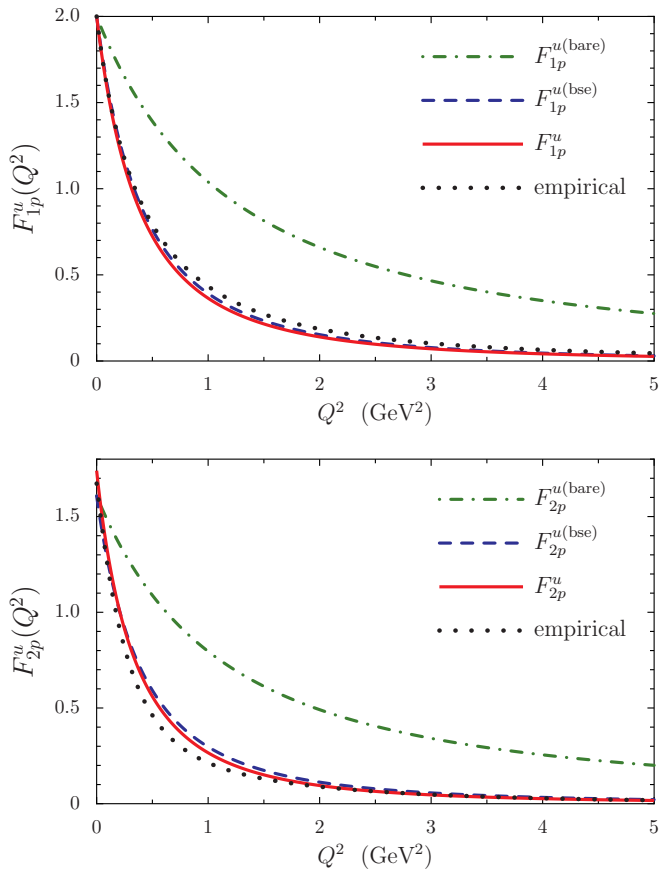

FIG. 24. (Color online) Proton up-quark-sector Dirac and Pauli form factors. The empirical results are obtained using Ref. [71] and Eq. (47).

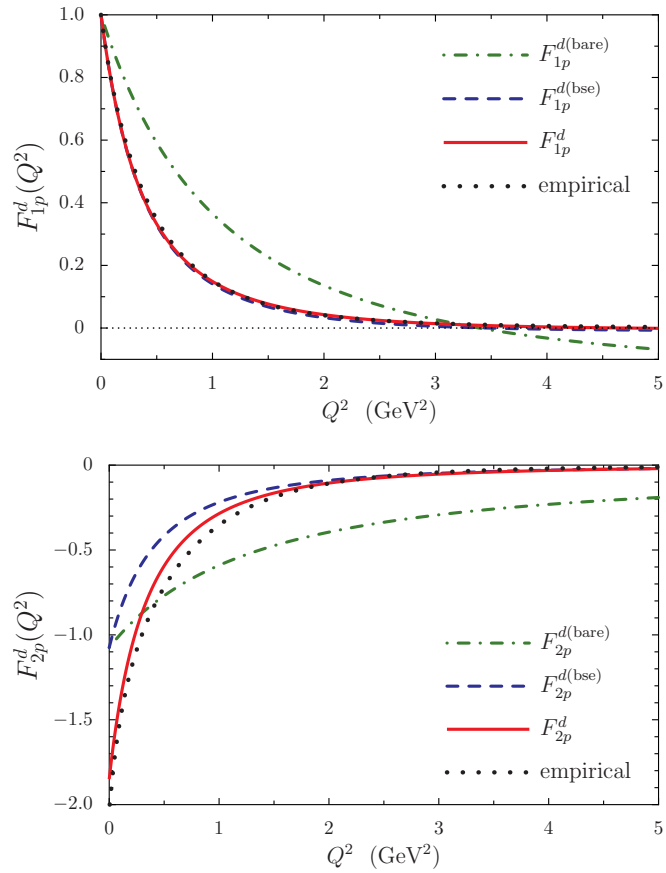

FIG. 25. (Color online) Proton down-quark-sector Dirac and Pauli form factors. The empirical results are obtained using Ref. [71] and Eq. (47).

TABLE VII. Results for the quark-sector contribution to the proton anomalous magnetic moments and radii, with constituent quark form factors given by Eqs. (61) and (105) [labeled with (bse)] and results that also include the pion cloud. The experimental values for the quark-sector anomalous magnetic moments and radii are obtained from from Ref. [71] using Eq. (47).

q	$\kappa^{q,(\mathrm{bse})}$	κ^{q}	$\kappa^{q,\mathrm{exp}}$	$r_E^{q,(\mathrm{bse})}$	r_E^{q}	$r_E^{q,\mathrm{exp}}$	$r_M^{q,(\mathrm{bse})}$	r_M^{q}	$r_E^{q,\mathrm{exp}}$
u sector	1.61	1.74	1.673	0.79	0.82	0.829 ± 0.097	0.77	0.83	0.816 ± 0.087
d sector	−1.07	−1.85	−2.033	0.75	0.71	0.720 ± 0.118	−0.53	0.98	1.048 ± 0.319

full results, which include pion loop effects, and the empirical parametrization is very good, for the u-quark sector we find that our Dirac form factor is slightly too soft and the Pauli form factor a little too hard. For the d quark sector the Dirac form factor is in excellent agreement with the empirical parametrization, whereas the Pauli form factor is slightly too soft. As we shall see, such small differences can produce apparently large effects in the combination required to compute G_E.

An interesting feature of these results is the role of the pionic corrections to the quark-sector Pauli form factors. In contrast to the usual proton and neutron Pauli form factors, which each receive significant corrections from the pion cloud, for the quark-sector form factors only F_{2p}^{d} receives sizable pionic corrections. For example, pion loop effects increase the magnitude of the d-sector anomalous magnetic moment by 73%, whereas the u quark sector only receives an 8% correction. This result is a consequence of the Pauli quark-sector form factors for the dressed quarks, where from Eq. (82) we see that the d-quark-sector contribution to the dressed-up quark anomalous magnetic moment has a magnitude 12 times larger than the u-sector contribution, and the proton consists of two dressed-up quarks and one dressed-down quark. When compared with experiment the d-sector anomalous magnetic moment is 10% too small and the u-sector 4% too large.

Table VII presents results for the quark sector contribution to the proton anomalous magnetic moments and radii. We find that the pion cloud has only a minor impact on the d-sector charge radius and the u-sector radii, whereas the d-sector magnetic radius actually changes sign once pion loop effects are included. Again, the origin of this lies with the large value of κ_U^d in Eq. (82). With pion cloud corrections included, all our results for the charge and magnetic quark-sector radii agree well with experiment.

Table VIII gives results for the Dirac and Pauli radii, defined by Eq. (48), for the proton and neutron and, for the proton, the corresponding quark-sector radii. The agreement with the empirical results of Ref. [71] is very good for the proton and neutron radii. For the proton quark-sector radii, the Dirac radii results are in good agreement; however, the u-quark-sector Pauli radius is slightly larger than experiment and the d-quark sector is 7% smaller.

Figures 26 and 27 present results for the total contribution of each diagram in Fig. 4 to the proton quark-sector form factors. That is, the proton quark-sector form factors are decomposed into

$$F_{ip}^{q} = F_{i\mathcal{Q},p}^{s,q} + F_{i\mathcal{Q},p}^{a,q} + F_{i\mathcal{D},p}^{s,q} + F_{i\mathcal{D},p}^{a,q} + F_{i\mathcal{D},p}^{sa,q}, \qquad (114)$$

where $i = (1, 2)$, $q = (u, d)$ and each function represents the total contribution to each quark sector for the Feynman diagrams in Fig. 4. Table IX gives results for the quark-sector diagrams of Fig. 4 evaluated at $Q^2 = 0$. For the Dirac form factors we see the dominance of the scalar diquark in the proton wave function, where these diagrams carry 69% of both the u and d quark-sector charges. Axial-vector diquarks also play an important role for the u-quark-sector form factors, carrying 26% of the charge and 35% of the anomalous magnetic moment. In the d-quark sector, $F_{2\mathcal{Q},p}^{s,d}$ would be zero without the effect of the pion cloud. The latter produces a contribution that constitutes 20% of the d-sector anomalous magnetic moment.

Recent accurate neutron form-factor data has enabled a precise experimental determination of the quark-sector proton form factors, using Eq. (44). The experimental quark-sector results from Ref. [56], along with our results, are presented in Fig. 28 for the Dirac form factors and in Fig. 29 for the Pauli form factors. *Prima facie*, these experimental results are remarkable. For Q^2 beyond 1–2-GeV^2 the d-quark sector of the proton Dirac form factor is much softer than the u quark sector. However, for the Pauli quark-sector form factors, it is the u-quark sector that is softer for low Q^2. However, at around $Q^2 \sim 1.5$ GeV^2 there is a crossover and the d-quark-sector form factor starts approaching zero more rapidly.

The empirical results illustrated in Fig. 28 are straightforward to understand within our framework. The dominant contributions to the quark-sector Dirac form factors come from the two Feynman diagrams which involve only a quark and a

TABLE VIII. Results for radii defined by Eq. (48) for the proton and neutron Dirac and Pauli form factors and for the quark-sector proton Dirac and Pauli form factors. In each case we show results where the dressed quark form factors are given by Eqs. (61) and (105) [labeled with (bse)] and results that also include the pion cloud. The empirical values are obtained from Ref. [71] and for the quark-sector results using Eq. (47).

	$r_1^{(\mathrm{bse})}$	r_1	r_1^{exp}	$r_2^{(\mathrm{bse})}$	r_2	r_2^{exp}		$r_1^{q,(\mathrm{bse})}$	r_1^{q}	$r_1^{q,\mathrm{exp}}$	$r_2^{q,(\mathrm{bse})}$	r_2^{q}	$r_2^{q,\mathrm{exp}}$
Proton	0.75	0.79	0.791	0.77	0.85	0.879	u sector	0.76	0.79	0.795	0.77	0.88	0.841
Neutron	0.20	0.09	0.119	0.76	0.88	0.911	d sector	0.80	0.80	0.809	0.76	0.88	0.938

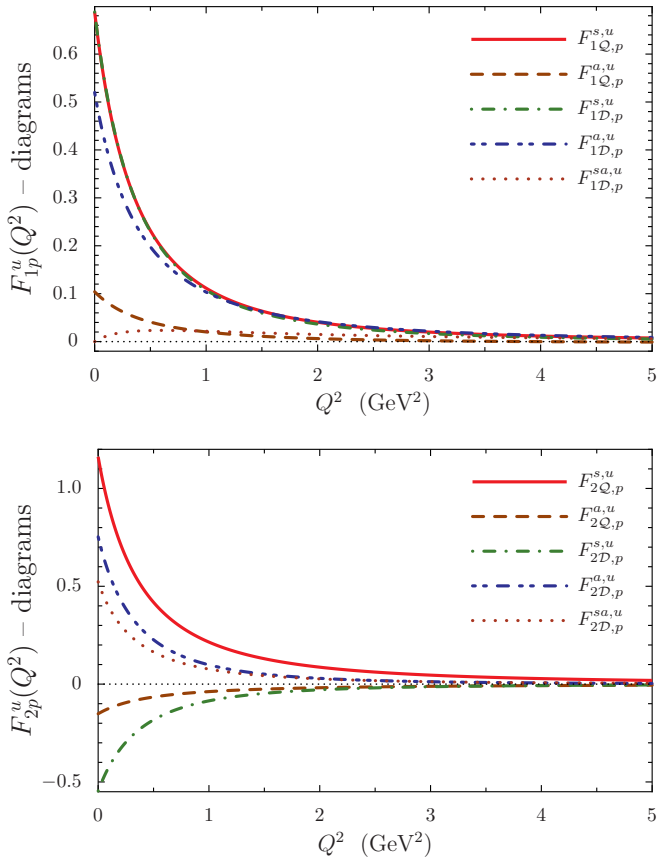

FIG. 26. (Color online) Total contributions to the proton u-sector form factors from each Feynman diagram in Fig. 4. These results include both the vector and the tensor coupling contributions and the sum gives the total u-sector Dirac and Pauli proton form factors (solid lines in Fig. 24).

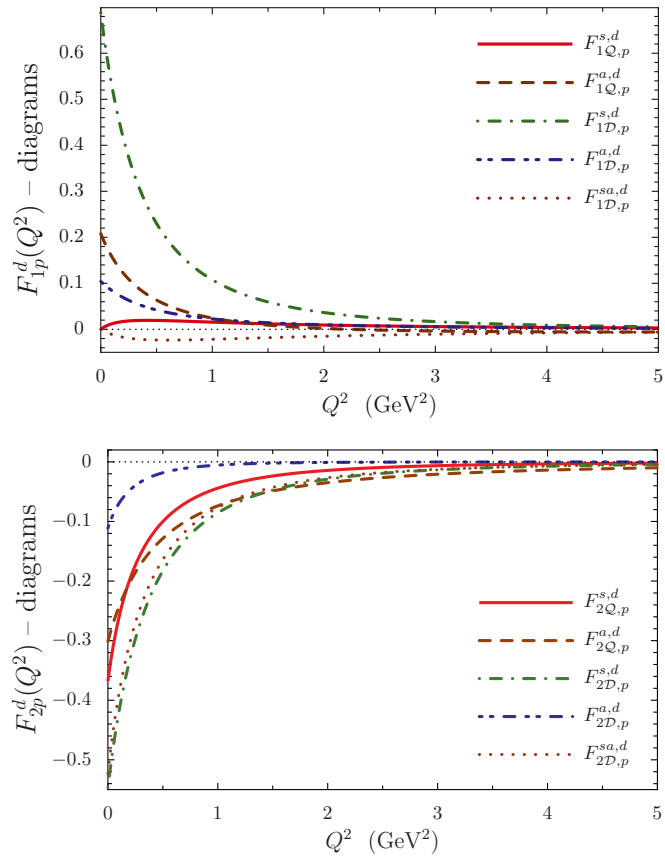

FIG. 27. (Color online) Total contributions to the proton d-sector form factors from each Feynman diagram in Fig. 4. These results include both the vector and the tensor coupling contributions and the sum gives the total d-sector Dirac and Pauli proton form factors (solid lines in Fig. 25).

scalar diquark. This is clear from the top panels of Figs. 26 and 27. The top panel in Figs. 10 demonstrates that the current d quarks that contribute to F^d_{1p} must primarily come from the dressed-down quark, and these contributions are suppressed by order $1/Q^2$ relative to the current u quarks from the quark diagram that contributes to F^u_{1p}. Thus, the dominance of scalar diquark correlations in the nucleon clearly provides a very natural explanation of the data in Fig. 28.

The zero crossing in our result for F^d_{1p} at $Q^2 \simeq 4.7$ GeV^2 is also straightforward to understand. We first note that the large Q^2 behavior of the form factors is governed by the quark diagrams in Fig. 4, because when the photon couples to a quark inside a diquark, the diquark form factors provide at least an additional factor of $1/Q^2$ relative to the quark diagrams. Considering only pointlike quarks, which is sufficient to study the large Q^2 behavior, we have for the proton quark-sector form factors

$$F^u_{ip} \overset{Q^2\to\infty}{\longrightarrow} f^{s,V}_{i\mathcal{Q}} + \tfrac{1}{3} f^{a,V}_{i\mathcal{Q}}, \tag{115}$$

$$F^d_{ip} \overset{Q^2\to\infty}{\longrightarrow} \tfrac{2}{3} f^{a,V}_{i\mathcal{Q}}, \tag{116}$$

where $i = (1, 2)$; cf. Eqs. (102) and (103). Therefore, the large Q^2 behavior of F^d_{1p} is governed by the nucleon body form factor $f^{a,V}_{1\mathcal{Q}}$ (see Fig. 18), which becomes negative at large Q^2

TABLE IX. Contributions to the nucleon quark-sector form factors from the various diagrams at $Q^2 = 0$. The vector contributions are obtained from the appropriate body form factors at $Q^2 = 0$ multiplied by isospin factors and quark charges. Therefore, these results do not change with the various approximations for the dressed quark form factors. The tensor contributions are only nonzero if the dressed quarks have an anomalous magnetic moment, and in this framework this occurs solely from pion loop effects. Rows with an entry of "0" are identically zero because of charge conservation.

q	$F^{s,q}_{1\mathcal{Q},p}$	$F^{a,q}_{1\mathcal{Q},p}$	$F^{s,q}_{1\mathcal{D},p}$	$F^{a,q}_{1\mathcal{D},p}$	$F^{sa,q}_{1\mathcal{D},p}$	F^q_{1p}	$F^{s,q}_{2\mathcal{Q},p}$	$F^{a,q}_{2\mathcal{Q},p}$	$F^{s,q}_{2\mathcal{D},p}$	$F^{a,q}_{2\mathcal{D},p}$	$F^{sa,q}_{2\mathcal{D},p}$	F^q_{2p}
u sector	0.69	0.10	0.69	0.52	0	2	1.16	−0.15	−0.55	0.75	0.52	1.73
d sector	0	0.21	0.69	0.10	0	1	−0.37	−0.30	−0.55	−0.11	−0.52	−1.85

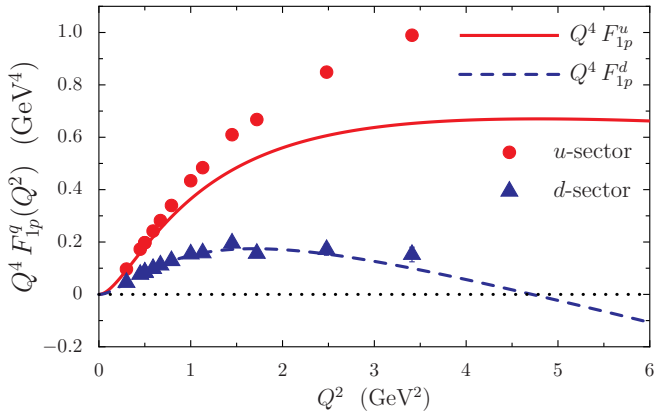

FIG. 28. (Color online) Quark-sector contributions to the proton Dirac form factor multiplied by Q^4. Experimental data are taken from Ref. [56].

and therefore F^d_{1p} has a zero crossing. Note that the empirical parametrizations of Ref. [71] also have a zero in F^d_{1p} at $Q^2 \simeq 7.9$ GeV^2.

Understanding the Q^2 dependence of the proton Pauli quark-sector form factors is more subtle within our model. Analogous to the Dirac form-factor example, F^u_{2p} receives a large contribution from the scalar quark diagram $f^{s,V}_{2Q}$; however, many other contributions are negative. In contrast, all diagrams add constructively to the F^d_{2p} form factor, which also receives a significant contribution from the pion cloud. Therefore, at low to moderate Q^2 we find $F^u_{2p}/\kappa_u \sim F^d_{2p}/\kappa_d$, with reasonable agreement with the data. However, at larger Q^2 the two quark diagrams in Eq. (115) partially cancel, giving $F^u_{2p}/\kappa_u < F^d_{2p}/\kappa_d$, which is opposite to the behavior observed in the data. The suppression of F^d_{2p} with respect to F^u_{2p} at large Q^2 was found in Ref. [76], where a major difference from the framework used here is that we make the static approximation to the quark exchange kernel and therefore exchange-type diagrams, as illustrated in Fig. 30, are absent from our form-factor calculation. This is the likely reason

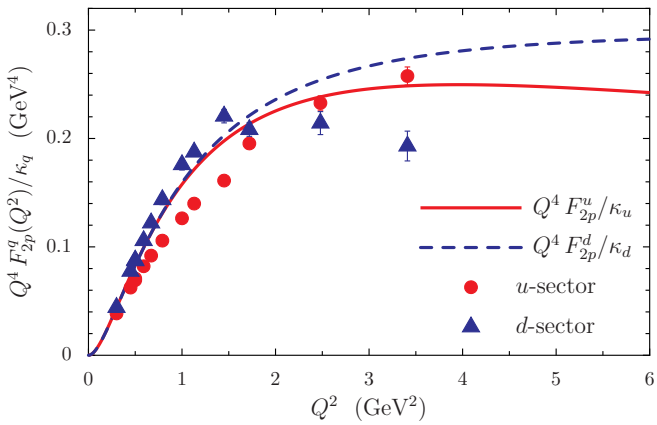

FIG. 29. (Color online) Quark-sector contributions to the proton Pauli form factor multiplied by Q^4. Experimental data are taken from Ref. [56].

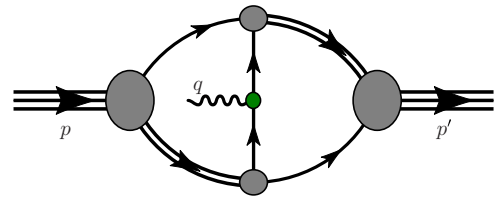

FIG. 30. (Color online) Exchange-type diagrams that do not appear in our present form-factor calculation because the static approximation is used for the quark exchange kernel.

for the discrepancy with experiment at large Q^2 observed in Fig. 29.

Detailed results for the proton and neutron Sachs form factors are given in Appendix C. Of contemporary interest is the proton Sachs form-factor ratio, G_{Ep}/G_{Mp}, for which our result is presented in Fig. 31. We find that this ratio decreases almost linearly with Q^2 but the slope we obtain is significantly larger than the experimental results obtained via the polarization transfer experiments, leading to a zero crossing at $Q^2 \approx 3.7$ GeV^2. So far no such zero crossing has been seen in the data but if it were to occur it would have to be in the domain $Q^2 \gtrsim 8$ GeV^2. The zero in the G_{Ep}/G_{Mp} ratio found here results from a zero in G_{Ep} and, as we have already noted, the cancellation between F_1 and F_2 in the linear combination needed for G_E means that even relatively small differences between the experimental and theoretical values of the individual from factors can be magnified there. We find that this zero actually arises from the u quark sector, as illustrated in the top panel of Fig. 33. This zero has its origin in the quark diagram with the scalar diquark spectator, which becomes negative at around $Q^2 \simeq 1.8$ GeV^2 and dominates at large Q^2. This can be seen in the top panel of Fig. 35. A possible reason for the discrepancy with data for the G_{Ep}/G_{Mp} ratio is the omission of exchange diagram contributions (illustrated in Fig. 30), which do not appear in the model described herein. The running of the quark mass function in QCD may also play an important role [77].

Results for the neutron Sachs form-factor ratio, G_{En}/G_{Mn}, are presented in Fig. 32. For $Q^2 \lesssim 1.5$ GeV^2 our results that

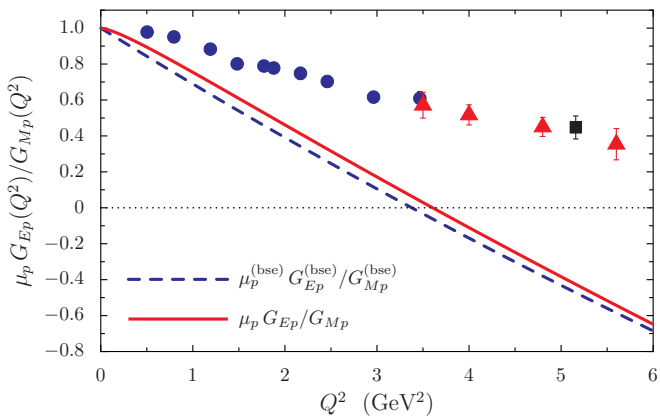

FIG. 31. (Color online) Proton Sachs form-factor ratio. Data are from Refs. [1–6].

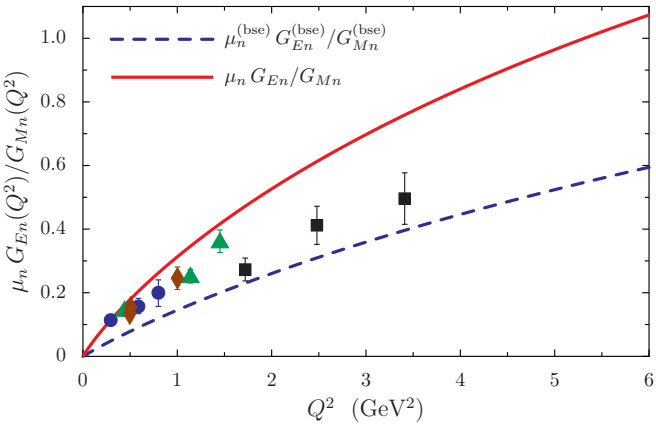

FIG. 32. (Color online) Neutron Sachs form-factor ratio. Data are from Ref. [78].

include pion loop corrections agree well with data. However, at larger Q^2 our ratio continues to grow too rapidly to be consistent with data. Our result for G_{En}/G_{Mn} does not possess a zero crossing for any Q^2 value. This is in contrast to the results of Ref. [76], which find a zero crossing at $Q^2 \simeq 11$ GeV^2.

VII. CONCLUSION

We have presented calculations of the nucleon form factors using a covariant and confining NJL model, which is a Poincaré covariant quantum field theory with many of the properties of QCD at low to moderate energies. The model satisfies current conservation exactly and because the framework is covariant the form factors are determined without the need to specify a reference frame. Poincaré covariance also demands nonzero quark orbital angular momentum in the proton wave function, and this is reflected in our results by large contributions to the nucleon Pauli form factors from quark-diquark components of the nucleon wave function that only carry charge (see Fig. 18 and related discussion).

A unique feature of these results is the parameter-free self-consistent inclusion of pion loop effects, as a perturbation to the "quark core" results obtained from the solution of a relativistic Faddeev equation. We find that these pion-cloud effects play a vital role for $Q^2 \lesssim 1$ GeV^2, which is consistent with earlier studies using chiral perturbation theory [79–85] and chiral extrapolation of lattice QCD data [86–89]. For example, in our calculation the pion cloud increases the magnitude of the proton and neutron anomalous magnetic moments by 25% and 45%, respectively, giving final results of $\kappa_p = 1.78$ and $\kappa_n = -1.81$, which are in rather good agreement with the empirical values.

In the limit of equal current quark masses our model satisfies charge symmetry and therefore the proton quark-sector form factors can be unambiguously determined. For the quark-sector radii we find that r_E^u is 16% larger than r_E^d, whereas for the magnetic radii r_M^d is 18% larger than r_M^u. The quark-sector magnetic radius result can be understood because pion loop effects induce a d-quark-sector anomalous magnetic moment for the dressed-up quark 12 times larger than the u quark-sector contribution. For the quark-sector form factors, pion-cloud effects are largely concentrated in the d-quark sector. For example, r_M^d actually changes sign when pionic effects are included and the value of $G_{Mp}^d(0)$ increases by a factor of ten because of pion loop effects.

An area of particular interest which has been identified in our study is the interplay between the respective roles of diquark correlations and pion effects. This is most dramatically illustrated by the comparison of Figs. 28 and 29. In the first we see the crucial importance on the behavior of the Dirac form factor of the dominance of scalar diquarks, when they can contribute. The smaller role of these scalar diquarks in the d-quark case naturally explains the suppression of the d-quark sector at larger values of the momentum transfer. On the other hand, in the case of the Pauli form factor the axial-vector diquarks and pion make significant contributions to the d-quark sector and this effectively counteracts the effect of the scalar diquark correlations. These are subtle but crucial aspects of the observed form factors.

Finally, looking to the future, an important near-term goal must be to apply the framework developed here to the study of nucleon transition form factors, for example, nucleon to Δ and nucleon to Roper transitions. This will elucidate the role of pion loop effects in these transitions and help to expose the nature of diquark correlations in the structure of baryons. The results presented herein and earlier work on nucleon PDFs [31,33] will also serve an a critical starting point for forthcoming studies of generalized PDFs [90,91].

ACKNOWLEDGMENTS

I.C.C. thanks Craig Roberts for many helpful discussions. This material is based upon work supported by the US Department of Energy, Office of Science, Office of Nuclear Physics, under Contract No. DE-AC02-06CH11357; the Australian Research Council through the ARC Centre of Excellence in Particle Physics at the Terascale and ARC Australian Laureate Fellowship No. FL0992247 (A.W.T.); and the Grant in Aid for Scientific Research (Kakenhi) of the Japanese Ministry of Education, Sports, Science and Technology, Project No. 20168769.

APPENDIX A: CONVENTIONS

We use the conventions of Ref. [92]. For example, the metric tensor has the form

$$g^{\mu\nu} = \text{diag}\,[1, -1, -1, -1] \tag{A1}$$

and the totally antisymmetric Levi-Civita tensor is normalized such that $\varepsilon^{0123} = 1$. Some important Dirac matrices are defined as

$$\gamma_5 = i\gamma^0\gamma^1\gamma^2\gamma^3 = -\frac{i}{4}\varepsilon_{\mu\nu\rho\sigma}\gamma^\mu\gamma^\nu\gamma^\rho\gamma^\sigma, \tag{A2}$$

$$\sigma^{\mu\nu} = \frac{i}{2}[\gamma^\mu, \gamma^\nu], \tag{A3}$$

and therefore

$$\text{Tr}[\gamma_5\gamma^\mu\gamma^\nu\gamma^\rho\gamma^\sigma] = -4i\,\varepsilon^{\mu\nu\rho\sigma} = 4i\,\varepsilon_{\mu\nu\rho\sigma}. \tag{A4}$$

APPENDIX B: PROOF OF ELECTROMAGNETIC GAUGE INVARIANCE

Electromagnetic gauge invariance manifests as electromagnetic current conservation, which for the nucleon is embodied in the statement

$$q_\mu\, j_N^\mu(p',p) = 0, \tag{B1}$$

where $q = p' - p$ and $j_N^\mu(p',p)$ is the nucleon electromagnetic current. The nucleon electromagnetic current is given by the six Feynman diagrams represented by Fig. 4 and therefore has the form

$$\begin{aligned} j_N^\mu(p',p) = {} & j_{\mathcal{Q}}^{s,\mu}(p',p) + j_{\mathcal{Q}}^{a,\mu}(p',p) + j_{\mathcal{D}}^{s,\mu}(p',p) \\ & + j_{\mathcal{D}}^{a,\mu}(p',p) + j_{\mathcal{D}}^{s\to a,\mu}(p',p) + j_{\mathcal{D}}^{a\to s,\mu}(p',p), \end{aligned} \tag{B2}$$

where the nomenclature is explained in Sec. VI. The individual Feynman diagram contributions to the nucleon electromagnetic current are

$$\begin{aligned} j_{\mathcal{Q}}^{s,\mu}(p',p) = {} & -Z_N\, \overline{\Gamma}_s \int \frac{d^4k}{(2\pi)^4} \\ & \times S(\ell')\, \Lambda_{\gamma Q}^\mu(\ell',\ell)\, S(\ell)\, \tau_s(k)\, \Gamma_s, \end{aligned} \tag{B3}$$

$$\begin{aligned} j_{\mathcal{Q}}^{a,\mu}(p',p) = {} & -Z_N\, \overline{\Gamma}_a^\alpha \int \frac{d^4k}{(2\pi)^4} \\ & \times S(\ell')\, \Lambda_{\gamma Q}^\mu(\ell',\ell)\, S(\ell)\, \tau_{a,\alpha\beta}(k)\, \Gamma_a^\beta, \end{aligned} \tag{B4}$$

$$\begin{aligned} j_{\mathcal{D}}^{s,\mu}(p',p) = {} & -Z_N\, i\overline{\Gamma}_s \int \frac{d^4k}{(2\pi)^4} \\ & \times S(k)\, \tau_s(\ell')\, \Lambda_s^\mu(\ell',\ell)\, \tau_s(\ell)\, \Gamma_s, \end{aligned} \tag{B5}$$

$$\begin{aligned} j_{\mathcal{D}}^{a,\mu}(p',p) = {} & -Z_N\, i\overline{\Gamma}_a^\lambda \int \frac{d^4k}{(2\pi)^4} \\ & \times S(k)\, \tau_{a,\lambda\beta}(\ell')\, \Lambda_a^{\mu,\alpha\beta}(\ell',\ell)\, \tau_{a,\alpha\sigma}(\ell)\, \Gamma_a^\sigma, \end{aligned} \tag{B6}$$

$$\begin{aligned} j_{\mathcal{D}}^{s\to a,\mu}(p',p) = {} & -Z_N\, i\overline{\Gamma}_a^\lambda \int \frac{d^4k}{(2\pi)^4} \\ & \times S(k)\, \tau_{a,\lambda\alpha}(\ell')\, \Lambda_{s\to a}^{\mu,\alpha}(\ell',\ell)\, \tau_s(\ell)\, \Gamma_s, \end{aligned} \tag{B7}$$

$$\begin{aligned} j_{\mathcal{D}}^{a\to s,\mu}(p',p) = {} & -Z_N\, i\overline{\Gamma}_s \int \frac{d^4k}{(2\pi)^4} \\ & \times S(k)\, \tau_s(\ell')\, \Lambda_{a\to s}^{\mu,\alpha}(\ell',\ell)\, \tau_{a,\alpha\lambda}(\ell)\, \Gamma_a^\lambda, \end{aligned} \tag{B8}$$

where $\ell' = p' - k$, $\ell = p - k$ and we have also dropped the momentum dependence of the Faddeev vertices. The quark-photon vertex is labeled by $\Lambda_{\gamma Q}^\mu$ and the various diquark-photon vertices are represented by Λ_s^μ, $\Lambda_a^{\mu,\alpha\beta}$, $\Lambda_{s\to a}^{\mu,\alpha}$, and $\Lambda_{a\to s}^{\mu,\alpha}$. These vertices satisfy the following Ward-Takahashi identities:

$$q_\mu\, \Lambda_{\gamma Q}^\mu(\ell',\ell) = \hat{Q}_q[S^{-1}(\ell') - S^{-1}(\ell)], \tag{B9}$$

$$q_\mu\, \Lambda_s^\mu(\ell',\ell) = -i\,\hat{Q}_s\big[\tau_s^{-1}(\ell') - \tau_s^{-1}(\ell)\big], \tag{B10}$$

$$q_\mu\, \Lambda_{a,ij}^{\mu,\alpha\beta}(\ell',\ell) = -i\,\hat{Q}_a^{ij}\big[\tau_a^{-1,\alpha\beta}(\ell') - \tau_a^{-1,\alpha\beta}(\ell)\big], \tag{B11}$$

$$q_\mu\, \Lambda_{s\to a}^{\mu,\alpha}(\ell',\ell) = 0, \tag{B12}$$

$$q_\mu\, \Lambda_{a\to s}^{\mu,\alpha}(\ell',\ell) = 0, \tag{B13}$$

where the charge operators have the form

$$\hat{Q}_q = \frac{1}{6} + \frac{\tau_3}{2}, \quad \hat{Q}_s = \frac{1}{3}, \quad \hat{Q}_a^{ij} = \frac{1}{3}\,\delta_{ij} + i\varepsilon_{ij3}. \tag{B14}$$

The indices on $\hat{Q}_a^{ij}$ represent isospin, where i is the initial diquark and j the final diquark. The contraction of the current with q_μ therefore gives

$$q_\mu\, j_{\mathcal{Q}}^{s,\mu} = -\hat{Q}_q\, \overline{\Gamma}_s \int_k [S(\ell') - S(\ell)]\tau_s(k)\, \Gamma_s, \tag{B15}$$

$$q_\mu\, j_{\mathcal{Q}}^{a,\mu} = -\hat{Q}_q\, \overline{\Gamma}_a^\alpha \int_k [S(\ell') - S(\ell)]\tau_{a,\alpha\beta}(k)\, \Gamma_a^\beta, \tag{B16}$$

$$q_\mu\, j_{\mathcal{D}}^{s,\mu} = -\hat{Q}_s \overline{\Gamma}_s \int_k S(k)[\tau_s(\ell') - \tau_s(\ell)]\, \Gamma_s, \tag{B17}$$

$$q_\mu\, j_{\mathcal{D}}^{a,\mu} = -\hat{Q}_a^{ij}\, \overline{\Gamma}_a^{\alpha,j} \int_k S(k)[\tau_{a,\alpha\beta}(\ell') - \tau_{a,\alpha\beta}(\ell)]\, \Gamma_a^{\beta,i}, \tag{B18}$$

where we have used $\tau_{a,\alpha\beta}\, \tau_a^{-1,\lambda\sigma} = \delta_{\alpha\lambda}\delta_{\beta\sigma}$. Therefore,

$$\begin{aligned} & q_\mu\, j_{\mathcal{Q}}^{s,\mu} + q_\mu\, j_{\mathcal{D}}^{s,\mu} \\ & \quad = -(\hat{Q}_q + \hat{Q}_s)\overline{\Gamma}_s(p')[\Pi_{Ns}(p') - \Pi_{Ns}(p)]\Gamma_s(p), \end{aligned} \tag{B19}$$

$$\begin{aligned} & q_\mu\, j_{\mathcal{Q}}^{a,\mu} + q_\mu\, j_{\mathcal{D}}^{a,\mu} \\ & \quad = -\big(\hat{Q}_q\, \delta^{ij} + \hat{Q}_a^{ij}\big)\overline{\Gamma}_a^{\alpha,j}(p')[\Pi_{Na,\alpha\beta}(p') \\ & \qquad - \Pi_{Na,\alpha\beta}(p)]\Gamma_a^{\beta,i}(p), \end{aligned} \tag{B20}$$

$$q_\mu\, j_{\mathcal{D}}^{s\to a,\mu} + q_\mu\, j_{\mathcal{D}}^{a\to s,\mu} = 0. \tag{B21}$$

In matrix notation we therefore have

$$q_\mu\, j_N^\mu = \overline{\Gamma}_N(p')\, \hat{Q}_N[\Pi_N(p') - \Pi_N(p)]\Gamma_N(p), \tag{B22}$$

where

$$\hat{Q}_N = \begin{bmatrix} \hat{Q}_q + \hat{Q}_s & 0 \\ 0 & \hat{Q}_q\, \delta^{ij} + \hat{Q}_a^{ij} \end{bmatrix}, \tag{B23}$$

and $\Pi_N(p)$ is defined in Eq. (37). It is straightforward to show

$$\hat{Q}_N\, \Gamma_N(p) = Q_N\, \Gamma_N(p), \tag{B24}$$

where

$$Q_N = \begin{cases} 1 & \text{proton,} \\ 0 & \text{neutron.} \end{cases} \tag{B25}$$

Therefore,

$$q_\mu\, j_N^\mu = Q_N\, \overline{\Gamma}_N(p')[\Pi_N(p') - \Pi_N(p)]\Gamma_N(p). \tag{B26}$$

The Faddeev equations for $\Gamma_N(p)$ and $\overline{\Gamma}_N(p)$ are

$$\Gamma_N(p) = Z\, \Pi_N(p)\, \Gamma_N(p), \tag{B27}$$

$$\overline{\Gamma}_N(p) = \overline{\Gamma}_N(p)\, \Pi_N(p)\, Z, \tag{B28}$$

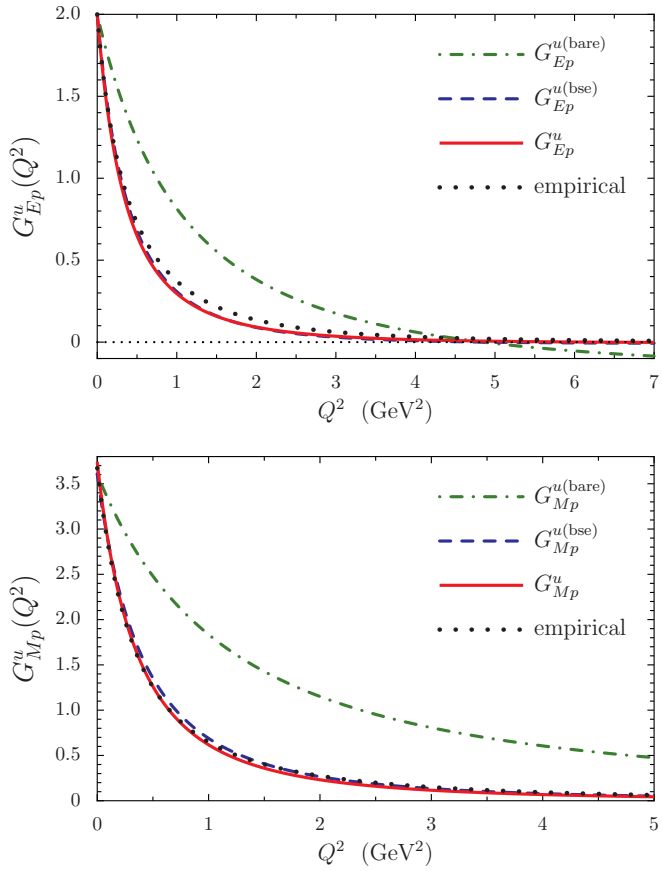

FIG. 33. (Color online) Proton up-quark-sector Sachs form factors. The empirical results are obtained using Ref. [71] and Eq. (47).

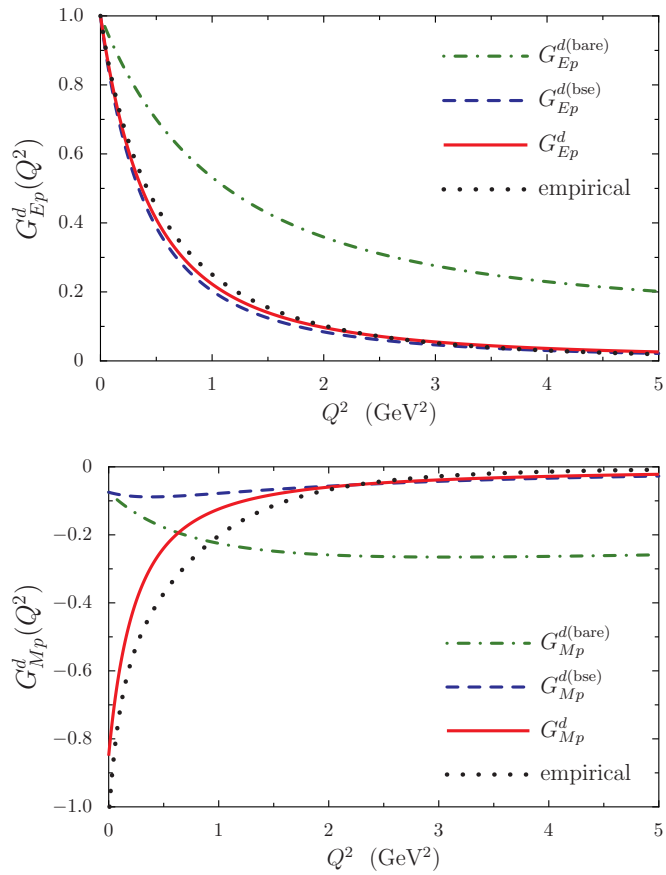

FIG. 34. (Color online) Neutron up-quark-sector Sachs form factors. The empirical results are obtained using Ref. [71] and Eq. (47).

where Z is the quark exchange kernel. Therefore,

$$q_\mu\, j^\mu_N = Q_N\, \overline{\Gamma}_N(p')[Z^{-1} - Z^{-1}]\Gamma_N(p) = 0, \qquad \text{(B29)}$$

as required by current conservation.

APPENDIX C: SACHS FORM FACTORS

In the nonrelativistic limit the electric and magnetic Sachs form factors are rigorously related to the charge and magnetization densities via a three-dimensional Fourier transform. In a Poincaré covariance quantum field theory this relation breaks down, but such a correspondence may still be a useful tool, at least for large distances. The Sachs form factors appear in the Rosenbluth parametrization of the elastic scattering differential cross section, given by

$$\frac{d\sigma}{d\Omega} = \frac{\sigma_{\mathrm{Mott}}}{1+\tau}\left[G_E^2(Q^2) + \frac{\tau}{\epsilon}\, G_M^2(Q^2)\right], \qquad \text{(C1)}$$

where $\tau = Q^2/(4\,M_N^2)$, σ_{Mott} represents that cross section for the scattering of the electron from a pointlike scalar particle, and ϵ is the longitudinal polarization of the virtual photon that mediates the interaction in Born approximation. For the Rosenbluth separation technique one considers the reduced cross section, namely,

$$\sigma_R \equiv \epsilon\, \frac{d\sigma}{d\Omega}\, \frac{1+\tau}{\sigma_{\mathrm{Mott}}} = \epsilon\, G_E^2(Q^2) + \tau\, G_M^2(Q^2). \qquad \text{(C2)}$$

Therefore, σ_R is linearly dependent on ϵ, so a linear fit to the reduced cross section at fixed Q^2 but a range of ϵ values gives $G_E^2(Q^2)$ as the slope and $\tau\, G_M^2(Q^2)$ as the y-axis intercept. At large Q^2 the reduced cross section is dominated by $\tau\, G_M^2(Q^2)$, making an accurate extraction of $G_E^2(Q^2)$ increasingly more difficult.

Our results for the proton and neutron Sachs form factors are presented in Figs. 22 and 23, where in each case we have used the three variants of dressed quark form factor discussed in Sec. IV. Empirical results from Ref. [71] are shown as the dotted lines. After including the vertex dressing from the BSE and also pion loop effects, the agreement with experiment is good. The proton electric form factor is slightly too soft and, as already discussed, possess a zero at $Q^2 \simeq 3.7$ GeV^2. For the proton magnetic form factor there is excellent agreement with the empirical results of Ref. [71]. Our result for the neutron electric form factor drops too slowly for $Q^2 \gtrsim 1$ GeV^2 and the magnetic form factor lacks a little strength for $Q^2 \lesssim 1$ GeV^2. However, overall the agreement with data is very good.

Results for the the proton quark sector Sachs form factors are given in Fig. 33 for the u-quark sector and Fig. 34 for the d-quark sector. Empirical results are obtained from Ref. [71] using the identities

$$G^u_{ip} = 2\,G_{ip} + G_{in}, \quad G^d_{ip} = G_{ip} + 2\,G_{in}, \qquad \text{(C3)}$$

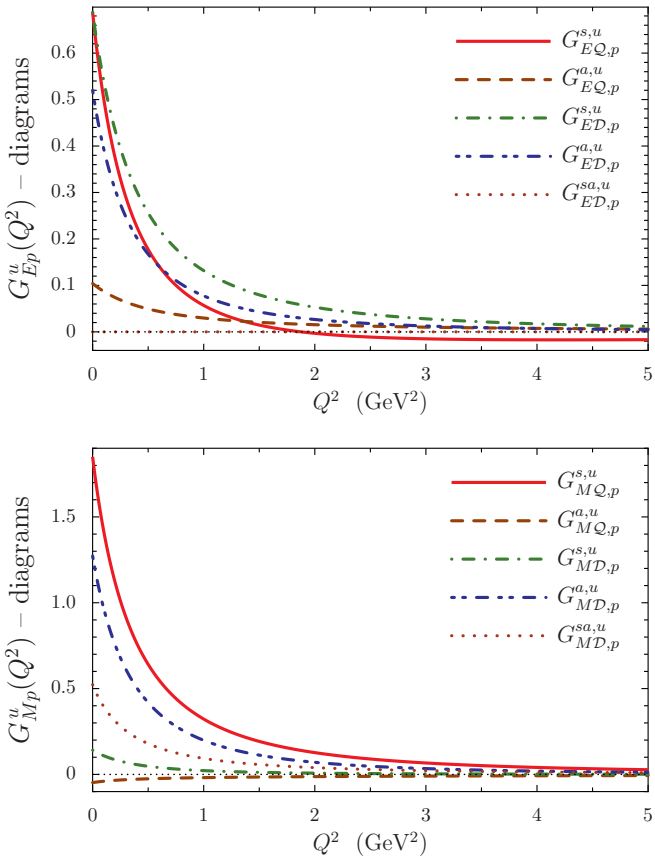

FIG. 35. (Color online) Total contributions to the proton u-sector Sachs form factors from each Feynman diagram in Fig. 4. These results include both the vector and the tensor coupling contributions and the sum gives the total u-sector Sachs proton form factors.

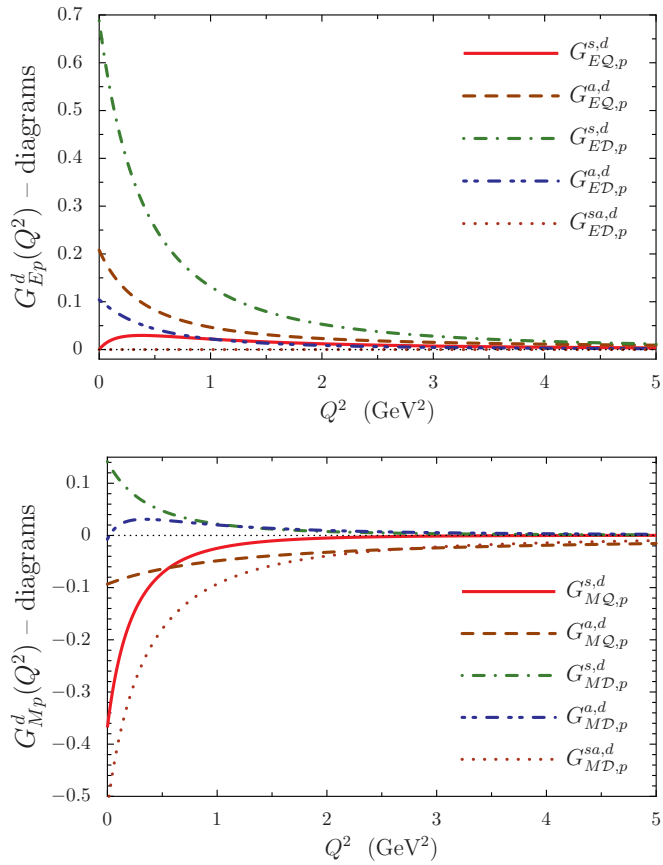

FIG. 36. (Color online) Total contributions to the neutron u-sector Sachs form factors from each Feynman diagram in Fig. 4. These results include both the vector and the tensor coupling contributions and the sum gives the total u-sector Sachs neutron form factors.

where $i = (E, M)$. Overall, the agreement with experiment is very good. Interestingly, however, the pion loop effects have little influence on the quark-sector Sachs form factors with the notable exception of $G^d_{Mp}(Q^2)$. Here the pion cloud results in a tenfold increase in the magnitude of the d-quark-sector magnetic moment, from $\mu_d^{(\mathrm{bse})} = -0.075\ \mu_N$ to $\mu_d = -0.85\ \mu_N$. There are a number of effects that all add to give this very large pion loop correction; most importantly, however, is the large d-quark-sector anomalous magnetic moment of a dressed-up quark [Eq. (82)] generated by the pion cloud. This results in a large contribution to $G^d_{Mp}(Q^2)$ from the quark diagram where the photon couples to a dressed-up quark, with a scalar diquark as spectator. Another notable result is that the zero in $G_{Ep}(Q^2)$ resides solely in the u-quark sector, as illustrated by the top panels of Figs. 33 and 34.

To understand these results better, we give the total contribution from each diagram, including both the BSE vertex dressing and pion loop effects in Fig. 35 for the u-quark sector and Fig. 36 for the d-quark sector. For the top panel in Figs. 35 it is clear that the zero in $G^u_{Ep}(Q^2)$ and therefore $G_{Ep}(Q^2)$ has its origin solely in $G^{s,u}_{EQ,p}$, the u-quark-sector contribution from quark diagrams with a spectator scalar diquark. We also find the interesting result that the diagrams associated with transitions between scalar and axial-vector diquarks are identically zero for the Sachs electric form factors but do contribute sizeably to the Sachs magnetic form factors.

APPENDIX D: ANALYSIS OF PION-CLOUD EFFECTS

A deeper understanding of our results is gained by decomposing the form factors in Figs. 20 and 21 into the various total contributions arising from each of the six diagrams represented in Fig. 4, for both the vector and tensor coupling to the dressed quarks. In this case the nucleon form factors are expressed as

$$F_{ip}(Q^2) = F^V_{ip}(Q^2) + F^T_{ip}(Q^2), \tag{D1}$$

$$F_{in}(Q^2) = F^V_{in}(Q^2) + F^T_{in}(Q^2), \tag{D2}$$

where $i = (1, 2)$. In terms of the six diagrams contained in Fig. 4 we have

$$F^V_{ip} = F^{s,V}_{iQ,p} + F^{a,V}_{iQ,p} + F^{s,V}_{iD,p} + F^{a,V}_{iD,p} + F^{sa,V}_{iD,p}, \tag{D3}$$

$$F^T_{ip} = F^{s,T}_{iQ,p} + F^{a,T}_{iQ,p} + F^{s,T}_{iD,p} + F^{a,T}_{iD,p} + F^{sa,T}_{iD,p}, \tag{D4}$$

and neutron expressions are obtained by $p \to n$. All terms in Eqs. (D3) and (D4) include the isospin coefficients and the dressed quark form factors.

Figures 37 and 38 illustrate the results for the total contributions from each diagram in Fig. 4 to the proton

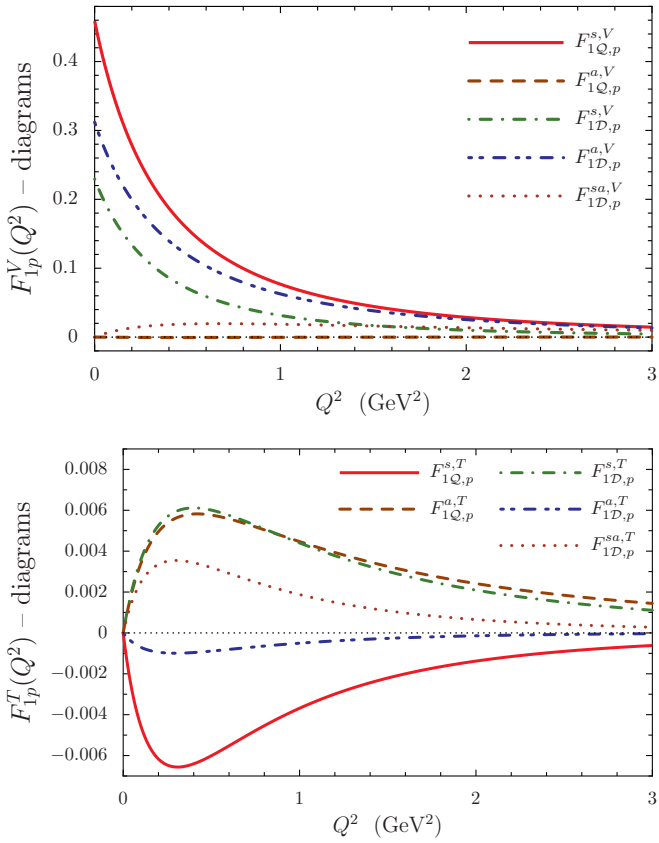

FIG. 37. (Color online) Total contributions to the proton Dirac form factor from each Feynman diagram in Fig. 4 for a vector coupling (top) and tensor coupling (bottom) to the dressed quarks. The sum of these ten contributions gives the total proton Dirac form factor illustrated in Fig. 20 (solid curve).

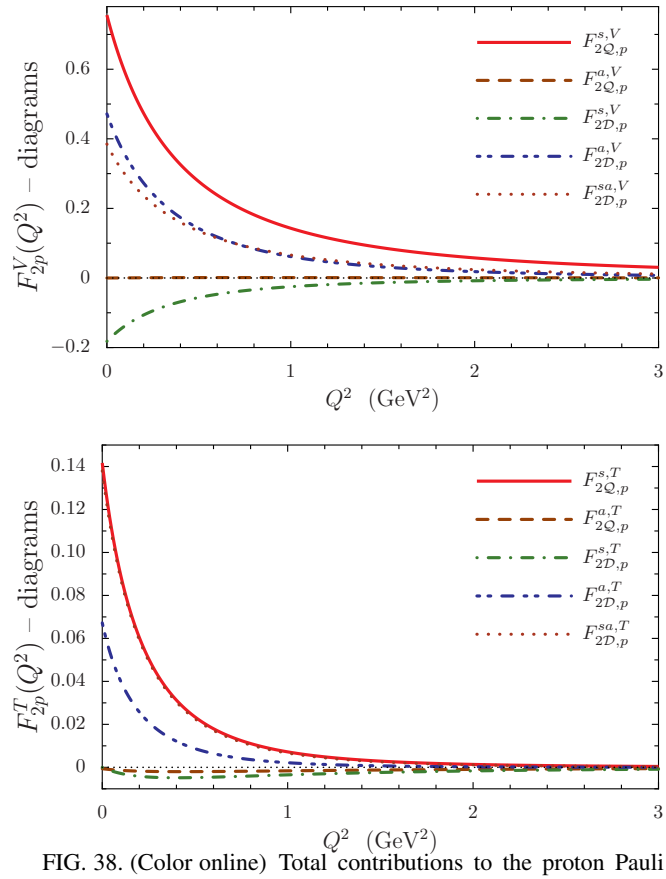

FIG. 38. (Color online) Total contributions to the proton Pauli form factor from each Feynman diagram in Fig. 4 for a vector coupling (top) and a tensor coupling (bottom) to the dressed quarks. The sum of these ten contributions gives the total proton Pauli form factor illustrated in Fig. 20 (solid curve).

form factors, where the contribution from the vector and tensor quark-photon couplings are shown separately. Results for the various contributions at $Q^2 = 0$ are also listed in rows 1 and 2 of Table X. These results demonstrate the dominance of the scalar diquark component in the proton wave function. For example, diagrams which contain only a scalar diquark carry 69% of the proton charge and 40% of its anomalous magnetic moment, while diagrams that contain only axial-vector diquarks carry 31% of the proton charge and 30% of its anomalous magnetic moment. The remainder of the anomalous magnetic moment, 30%, is carried by diagrams with both scalar and axial-vector diquarks. The contributions that arise from the tensor coupling to the dressed quarks, illustrated in the bottom panels of Figs. 37 and 38, diminish rapidly with increasing Q^2 because they are suppressed by the dressed quark Pauli form factors, illustrated in Fig. 6, which vanish monotonically for increasing Q^2.

The coupling of the photon to the diquarks is not only necessary for charge conservation, but is critical for a good description of the experimental data. Here the axial-vector diquarks play an important role. For a proton, the photon

TABLE X. Total contributions to the nucleon Dirac and Pauli form factors from the various diagrams at $Q^2 = 0$. The vector contributions are obtained from the appropriate body form factors at $Q^2 = 0$ multiplied by isospin factors and quark charges. Therefore, the vector results do not change with the various approximations for the dressed quark form factors. The tensor contributions are only nonzero if the dressed quarks have an anomalous magnetic moment, and in this framework this occurs solely from pion loop effects. Rows with an entry of "0" are identically zero because of charge conservation.

	$F_{1\mathcal{Q}}^{s,V}$	$F_{1\mathcal{Q}}^{a,V}$	$F_{1\mathcal{D}}^{s,V}$	$F_{1\mathcal{D}}^{a,V}$	$F_{1\mathcal{D}}^{sa,V}$	$F_{1\mathcal{Q}}^{s,T}$	$F_{1\mathcal{Q}}^{a,T}$	$F_{1\mathcal{D}}^{s,T}$	$F_{1\mathcal{D}}^{a,T}$	$F_{1\mathcal{D}}^{sa,T}$	Total
F_{1p}	0.46	0	0.23	0.31	0	0	0	0	0	0	1
F_{2p}	0.76	0	−0.18	0.47	0.38	0.14	0.0	0.0	0.07	0.14	1.78
F_{1n}	−0.23	0.10	0.23	−0.10	0	0	0	0	0	0	0
F_{2n}	−0.38	−0.15	−0.18	−0.16	−0.38	−0.25	0.0	0.0	−0.17	−0.14	−1.81

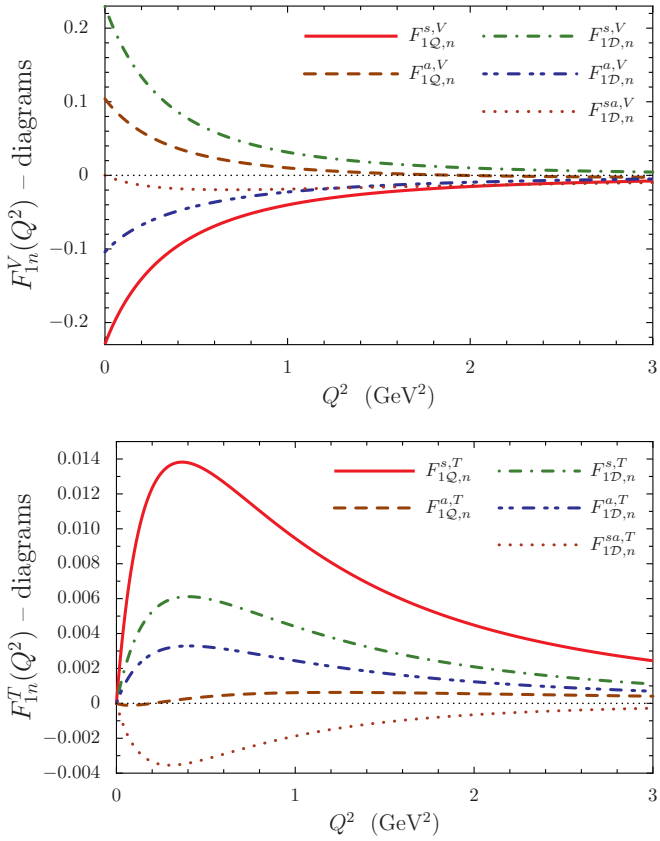

FIG. 39. (Color online) Total contributions to the neutron Dirac form factor from each Feynman diagram in Fig. 4 for a vector quark coupling (top) and tensor quark coupling (bottom). The sum of these ten contributions gives the total neutron Dirac form factor illustrated in Fig. 21 (solid curve).

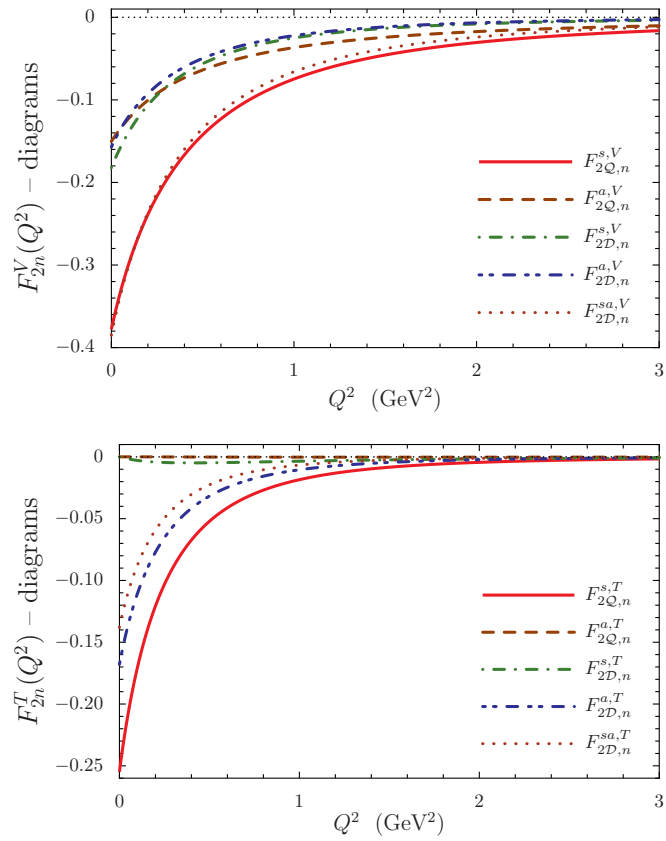

FIG. 40. (Color online) Total contributions to the neutron Pauli form factor from each Feynman diagram in Fig. 4 for a vector quark coupling (top) and tensor quark coupling (bottom). The sum of these ten contributions gives the total neutron Dirac form factor illustrated in Fig. 21 (solid curve).

is twice as likely to couple to a $\{uu\}$ type axial-vector diquark than one of type $\{ud\}$. Furthermore, axial-vector diquarks of type $\{uu\}$ have a charge of 4/3 and a magnetic moment of 3.27 μ_N (see Table III) and hence they provide the second-largest contribution to the proton charge and anomalous magnetic moment. The largest contribution in each case comes from the quark diagram with a spectator scalar diquark. With the exception of the diquark diagram with an axial-vector diquark spectator, the Feynman diagrams of Fig. 4, for the vector coupling, can only contribute to $F_{2p}(Q^2)$ if the quarks have nonzero orbital angular momentum. The sizable contributions from all other diagrams (see Fig. 38) indicate that there is significant quark orbital angular momentum in the proton wave function [93,94].

Figures 39 and 40 and rows 3 and 4 of Table X give results for the neutron form factors, broken down into the total vector and tensor coupling contributions from the Feynman diagrams of Fig. 4. For the Dirac form factor the diagram pairs with the same quark-diquark structure cancel each other to give a charge of zero, while diagrams that contain only scalar diquarks carry 45% of the neutron anomalous magnetic moment and diagrams containing only axial-vector diquarks carry 27%. The remaining 28% is carried by diagrams with both scalar and axial-vector diquarks. The tensor coupling contributions to $F_{1n}(Q^2)$ are much more significant compared to the proton case, an indication of the particular sensitivity of the neutron Dirac form factor to pion-cloud effects. Axial-vector diquarks play a reduced role in neutron structure, compared to the proton, because the $\{dd\}$-type axial-vector diquark has half the charge and an anomalous magnetic moment 65% the size of the $\{uu\}$-type diquark found in the proton.

[1] M. K. Jones *et al.* (Jefferson Lab Hall A Collaboration), Phys. Rev. Lett. **84**, 1398 (2000).
[2] O. Gayou *et al.* (Jefferson Lab Hall A Collaboration), Phys. Rev. Lett. **88**, 092301 (2002).
[3] O. Gayou, K. Wijesooriya, A. Afanasev, M. Amarian, K. Aniol, S. Becher, K. Benslama, L. Bimbot *et al.*, Phys. Rev. C **64**, 038202 (2001).
[4] V. Punjabi, C. F. Perdrisat, K. A. Aniol, F. T. Baker, J. Berthot, P. Y. Bertin, W. Bertozzi, A. Besson *et al.*, Phys. Rev. C **71**, 055202 (2005); **71**, 069902(E) (2005).

[5] A. J. R. Puckett, E. J. Brash, M. K. Jones, W. Luo, M. Meziane, L. Pentchev, C. F. Perdrisat, V. Punjabi *et al.*, Phys. Rev. Lett. **104**, 242301 (2010).
[6] A. J. R. Puckett, E. J. Brash, O. Gayou, M. K. Jones, L. Pentchev, C. F. Perdrisat, V. Punjabi, K. A. Aniol *et al.*, Phys. Rev. C **85**, 045203 (2012).
[7] S. J. Brodsky and G. R. Farrar, Phys. Rev. Lett. **31**, 1153 (1973).
[8] S. J. Brodsky and G. R. Farrar, Phys. Rev. D **11**, 1309 (1975).
[9] J. P. Ralston and P. Jain, Phys. Rev. D **69**, 053008 (2004).
[10] R. Pohl, A. Antognini, F. Nez, F. D. Amaro, F. Biraben, J. M. R. Cardoso, D. S. Covita, A. Dax *et al.*, Nature (London) **466**, 213 (2010).
[11] A. Antognini, F. Nez, K. Schuhmann, F. D. Amaro, F. Biraben, J. M. R. Cardoso, D. S. Covita, A. Dax *et al.*, Science **339**, 417 (2013).
[12] I. C. Cloët and G. A. Miller, Phys. Rev. C **83**, 012201 (2011).
[13] G. A. Miller, A. W. Thomas, J. D. Carroll, and J. Rafelski, Phys. Rev. A **84**, 020101 (2011).
[14] J. D. Carroll, A. W. Thomas, J. Rafelski, and G. A. Miller, Phys. Rev. A **84**, 012506 (2011).
[15] V. N. Gribov and L. N. Lipatov, Yad. Fiz. **15**, 1218 (1972) [Sov. J. Nucl. Phys. **15**, 675 (1972)].
[16] G. Altarelli and G. Parisi, Nucl. Phys. B **126**, 298 (1977).
[17] Y. L. Dokshitzer, Zh. Eksp. Teor. Fiz. **73**, 1216 (1977) [Sov. Phys. JETP **46**, 641 (1977)].
[18] Y. Nambu and G. Jona-Lasinio, Phys. Rev. **122**, 345 (1961).
[19] Y. Nambu and G. Jona-Lasinio, Phys. Rev. **124**, 246 (1961).
[20] U. Vogl and W. Weise, Prog. Part. Nucl. Phys. **27**, 195 (1991).
[21] T. Hatsuda and T. Kunihiro, Phys. Rep. **247**, 221 (1994).
[22] S. P. Klevansky, Rev. Mod. Phys. **64**, 649 (1992).
[23] A. W. Thomas, S. Theberge, and G. A. Miller, Phys. Rev. D **24**, 216 (1981).
[24] S. Theberge and A. W. Thomas, Nucl. Phys. A **393**, 252 (1983).
[25] A. W. Thomas, Adv. Nucl. Phys. **13**, 1 (1984).
[26] N. Ishii, W. Bentz, and K. Yazaki, Phys. Lett. B **301**, 165 (1993).
[27] N. Ishii, W. Bentz, and K. Yazaki, Phys. Lett. B **318**, 26 (1993).
[28] N. Ishii, W. Bentz, and K. Yazaki, Nucl. Phys. A **587**, 617 (1995).
[29] H. Mineo, W. Bentz, N. Ishii, A. W. Thomas, and K. Yazaki, Nucl. Phys. A **735**, 482 (2004).
[30] I. C. Cloët, W. Bentz, and A. W. Thomas, Phys. Rev. Lett. **95**, 052302 (2005).
[31] I. C. Cloët, W. Bentz, and A. W. Thomas, Phys. Lett. B **621**, 246 (2005).
[32] I. C. Cloët, W. Bentz, and A. W. Thomas, Phys. Lett. B **642**, 210 (2006).
[33] I. C. Cloët, W. Bentz, and A. W. Thomas, Phys. Lett. B **659**, 214 (2008).
[34] T. Ito, W. Bentz, I. C. Cloët, A. W. Thomas, and K. Yazaki, Phys. Rev. D **80**, 074008 (2009).
[35] H. H. Matevosyan, A. W. Thomas, and W. Bentz, Phys. Rev. D **83**, 074003 (2011).
[36] H. H. Matevosyan, W. Bentz, I. C. Cloët, and A. W. Thomas, Phys. Rev. D **85**, 014021 (2012).
[37] H. H. Matevosyan, A. W. Thomas, and W. Bentz, Phys. Rev. D **86**, 034025 (2012).
[38] W. Bentz and A. W. Thomas, Nucl. Phys. A **696**, 138 (2001).
[39] M. Buballa, Phys. Rep. **407**, 205 (2005).
[40] D. Ebert, T. Feldmann, and H. Reinhardt, Phys. Lett. B **388**, 154 (1996).
[41] G. Hellstern, R. Alkofer, and H. Reinhardt, Nucl. Phys. A **625**, 697 (1997).
[42] P. Maris and C. D. Roberts, Int. J. Mod. Phys. E **12**, 297 (2003).
[43] H. L. L. Roberts, L. Chang, I. C. Cloët, and C. D. Roberts, Few Body Syst. **51**, 1 (2011).
[44] F. E. Close and A. W. Thomas, Phys. Lett. B **212**, 227 (1988).
[45] A. W. Schreiber, P. J. Mulders, A. I. Signal, and A. W. Thomas, Phys. Rev. D **45**, 3069 (1992).
[46] M. Hess, F. Karsch, E. Laermann, and I. Wetzorke, Phys. Rev. D **58**, 111502 (1998).
[47] A. Bender, C. D. Roberts, and L. Von Smekal, Phys. Lett. B **380**, 7 (1996).
[48] A. Buck, R. Alkofer, and H. Reinhardt, Phys. Lett. B **286**, 29 (1992).
[49] H. Mineo, W. Bentz, and K. Yazaki, Phys. Rev. C **60**, 065201 (1999).
[50] H. Mineo, W. Bentz, N. Ishii, and K. Yazaki, Nucl. Phys. A **703**, 785 (2002).
[51] F. J. Ernst, R. G. Sachs, and K. C. Wali, Phys. Rev. **119**, 1105 (1960).
[52] R. D. Young, J. Roche, R. D. Carlini, and A. W. Thomas, Phys. Rev. Lett. **97**, 102002 (2006).
[53] K. A. Aniol *et al.* (HAPPEX Collaboration), Phys. Rev. Lett. **96**, 022003 (2006).
[54] D. S. Armstrong *et al.* (G0 Collaboration), Phys. Rev. Lett. **95**, 092001 (2005).
[55] S. Baunack, K. Aulenbacher, D. Balaguer Rios, L. Capozza, J. Diefenbach, B. Glaser, D. von Harrach, Y. Imai *et al.*, Phys. Rev. Lett. **102**, 151803 (2009).
[56] G. D. Cates, C. W. de Jager, S. Riordan, and B. Wojtsekhowski, Phys. Rev. Lett. **106**, 252003 (2011).
[57] T. Horikawa and W. Bentz, Nucl. Phys. A **762**, 102 (2005).
[58] P. Maris and P. C. Tandy, Phys. Rev. C **61**, 045202 (2000).
[59] S. R. Amendolia *et al.* (NA7 Collaboration), Nucl. Phys. B **277**, 168 (1986).
[60] S. R. Amendolia, B. Badelek, G. Batignani, G. A. Beck, F. Bedeschi, E. H. Bellamy, E. Bertolucci, D. Bettoni *et al.*, Phys. Lett. B **146**, 116 (1984).
[61] T. Horn *et al.* (Jefferson Lab F(pi)-2 Collaboration), Phys. Rev. Lett. **97**, 192001 (2006).
[62] V. Tadevosyan *et al.* (Jefferson Lab F(pi) Collaboration), Phys. Rev. C **75**, 055205 (2007).
[63] H. P. Blok *et al.* (Jefferson Lab Collaboration), Phys. Rev. C **78**, 045202 (2008).
[64] G. P. Lepage and S. J. Brodsky, Phys. Lett. B **87**, 359 (1979).
[65] G. R. Farrar and D. R. Jackson, Phys. Rev. Lett. **43**, 246 (1979).
[66] M. Gluck, E. Reya, and A. Vogt, Eur. Phys. J. C **5**, 461 (1998).
[67] L. Chang, I. C. Cloët, C. D. Roberts, S. M. Schmidt, and P. C. Tandy, Phys. Rev. Lett. **111**, 141802 (2013).
[68] E. B. Dally, J. M. Hauptman, J. Kubic, D. H. Stork, A. B. Watson, Z. Guzik, T. S. Nigmanov, V. D. Ryabtsov *et al.*, Phys. Rev. Lett. **48**, 375 (1982).
[69] L. L. Frankfurt and M. I. Strikman, Nucl. Phys. B **148**, 107 (1979).
[70] S. J. Brodsky and J. R. Hiller, Phys. Rev. D **46**, 2141 (1992).
[71] J. J. Kelly, Phys. Rev. C **70**, 068202 (2004).
[72] J. Beringer *et al.* (Particle Data Group Collaboration), Phys. Rev. D **86**, 010001 (2012).
[73] X. Zhan, K. Allada, D. S. Armstrong, J. Arrington, W. Bertozzi, W. Boeglin, J.-P. Chen, and K. Chirapatpimol *et al.*, Phys. Lett. B **705**, 59 (2011).

[74] J. C. Bernauer *et al.* (A1 Collaboration), Phys. Rev. Lett. **105**, 242001 (2010).
[75] I. Sick, Prog. Part. Nucl. Phys. **67**, 473 (2012).
[76] I. C. Cloët, G. Eichmann, B. El-Bennich, T. Klahn, and C. D. Roberts, Few Body Syst. **46**, 1 (2009).
[77] I. C. Cloët, C. D. Roberts, and A. W. Thomas, Phys. Rev. Lett. **111**, 101803 (2013).
[78] S. Riordan, S. Abrahamyan, B. Craver, A. Kelleher, A. Kolarkar, J. Miller, G. D. Cates, N. Liyanage *et al.*, Phys. Rev. Lett. **105**, 262302 (2010).
[79] E. E. Jenkins, M. E. Luke, A. V. Manohar, and M. J. Savage, Phys. Lett. B **302**, 482 (1993); **388**, 866(E) (1996).
[80] U. G. Meissner and S. Steininger, Nucl. Phys. B **499**, 349 (1997).
[81] D. Arndt and B. C. Tiburzi, Phys. Rev. D **69**, 014501 (2004).
[82] M. Göckeler, T. R. Hemmert, R. Horsley, D. Pleiter, P. E. L. Rakow, A. Schäfer, and G. Schierholz (QCDSF Collaboration), Phys. Rev. D **71**, 034508 (2005).
[83] L. S. Geng, J. Martin Camalich, and M. J. Vicente Vacas, Phys. Rev. D **80**, 034027 (2009).
[84] V. Lensky and V. Pascalutsa, Pisma Zh. Eksp. Teor. Fiz. **89**, 127 (2009) [JETP Lett. **89**, 108 (2009)].
[85] T. Bauer, J. C. Bernauer, and S. Scherer, Phys. Rev. C **86**, 065206 (2012).
[86] P. Wang, D. B. Leinweber, A. W. Thomas, and R. D. Young, Phys. Rev. D **75**, 073012 (2007).
[87] R. D. Young, D. B. Leinweber, and A. W. Thomas, Phys. Rev. D **71**, 014001 (2005).
[88] P. E. Shanahan, A. W. Thomas, R. D. Young, J. M. Zanotti, R. Horsley, Y. Nakamura, D. Pleiter, P. E. L. Rakow *et al.*, Phys. Rev. D **90**, 034502 (2014).
[89] P. E. Shanahan, A. W. Thomas, R. D. Young, J. M. Zanotti, R. Horsley, Y. Nakamura, D. Pleiter, P. E. L. Rakow *et al.*, Phys. Rev. D **89**, 074511 (2014).
[90] M. Diehl, Phys. Rep. **388**, 41 (2003).
[91] A. V. Belitsky and A. V. Radyushkin, Phys. Rep. **418**, 1 (2005).
[92] C. Itzykson and J.-B. Zuber, *Quantum Field Theory*, International Series in Pure and Applied Physics (McGraw-Hill, New York, 1980), p. 705.
[93] F. Myhrer and A. W. Thomas, Phys. Lett. B **663**, 302 (2008).
[94] A. W. Thomas, Phys. Rev. Lett. **101**, 102003 (2008).